

Lawrence Berkeley National Laboratory

Recent Work

Title

Finite-element analysis of top-casing electric source method for imaging hydraulically active fracture zones

Permalink

<https://escholarship.org/uc/item/8qr486nz>

Journal

Geophysics, 84(1)

ISSN

0016-8033

Authors

Um, ES
Kim, J
Wilt, MJ
[et al.](#)

Publication Date

2019

DOI

10.1190/geo2018-0451.1

Peer reviewed

**1FINITE ELEMENT ANALYSIS OF TOP-CASING ELECTRIC SOURCE METHOD FOR
2IMAGING HYDRAULICALLY-ACTIVE FRACTURE ZONES**

3

4

5

6

7

8

9

10LIST OF AUTHORS:

11Evan Schankee Um, Earth and Environmental Sciences Area, Lawrence Berkeley National Laboratory,
12evanum@gmail.com and esum@lbl.gov

13Jihoon Kim, Harold Vance Department of Petroleum Engineering, Texas A&M University,
14jihoon.kim@tamu.edu

15Michael J. Wilt, Earth and Environmental Sciences Area, Lawrence Berkeley National Laboratory,
16mwilt@lbl.gov

17Michael Commer, Earth and Environmental Sciences Area, Lawrence Berkeley National Laboratory,
18mcommer@lbl.gov

19Seung-Sep Kim, Department of Geology and Earth Environmental Sciences, Chungnam National
20University, Daejeon, South Korea, seungsep@cnu.ac.kr

21 **ABSTRACT**

22 Imaging hydraulically-active fracture zones (HAFZ) is of paramount importance to subsurface resource
23 extraction, geological storage and hazardous waste disposal. We present advanced 3D finite-element (FE)
24 electrical imaging algorithms for HAFZ in the presence of a steel-cased well. The algorithms employ
25 tetrahedral FE meshes in the simulation domain and coarse rectangular finite-difference (FD) meshes in
26 the imaging domain. This heterogeneous dual-mesh approach is well suited to modeling multi-scale earth
27 model due to steel-cased wells. We show that the algorithms accurately and efficiently simulate surface
28 electric field measurements over a 3D HAFZ at depth when one end point of a surface electric source is
29 connected to a wellhead. For brevity, this configuration is called the top-casing electric source method. By
30 replacing a hollow cased well with a solid prism, we improve our computational efficiency without
31 affecting the solution accuracy. The sensitivity of the top-casing source method to HAFZ highly depends
32 on the continuity of a steel-cased well, because it makes currents preferentially flow to HAFZ. The
33 sensitivity also depends on conductivity structures around the well because they control current leaking
34 from the steel-cased well. We show that the method can image a localized HAFZ and detect changes in its
35 width and height. The imaging results are improved when a volume of the imaging domain is constrained
36 from geomechanical perspectives. A primary advantage of the method is the fact that both sources and
37 receivers are placed on the surface, thus not interrupting well operation.

38 **INTRODUCTION**

39 Imaging hydraulically active fracture zones (HAFZ) is an important topic in applied geophysics. For
40 example, hydraulic fracturing and stimulation have been widely used for enhancing production in oil, gas
41 and geothermal fields (Zoback 2007; Zoback et. al. 2010). Traditional borehole methods are sensitive to
42 deep HAFZ, but their sensitivity is often limited to the vicinity of the well. Thus, they cannot tell us about
43 an overall hydraulically stimulated volume of subsurface. The most often used method for characterizing
44 HAFZ in a reservoir scale would be micro-earthquake (MEQ) methods (Warpinski et al. 2005; Vermilyen

45and Zoback, 2011). By analyzing MEQ event locations, we can estimate the stimulation volume.
46However, MEQ-based mapping highly depends on initial velocity models, which we do not know well,
47leaving uncertainties. More importantly, MEQ event locations do not necessarily correlate with active
48fluid pathways and thus, provide only a portion of the answer about estimating overall HAFZ (Hoversten
49et al, 2015).

50 It is also important to image deep HAFZ in geological storage sites such as CO₂ sequestration and
51hazardous waste disposal sites. During their injection phase, MEQ events are often recorded and can be
52utilized for imaging fluid movements and monitoring potential leakage. However, after the injection
53phase, the magnitudes of MEQ are often too small to be reliably recorded and interpreted in practice
54(Johnston and Shralow, 2011). Active-source seismic methods can also be considered an effective tool for
55the monitoring goal. However, their major limitation is long acquisition time and high processing cost.

56 Electrical and electromagnetic (EM) methods are sensitive to pore fluids and thus have the potential to
57directly sense a HAFZ, complementing MEQ and active source seismic monitoring. To ensure the
58sufficient sensitivity of the methods to deep HAFZ, one can consider injecting highly-conductive saline
59fluid or fluid with electromagnetically contrasting tracers (e.g. Moridis and Oldenburg, 2001; Rahmani et
60al., 2014; Kim et al., 2014). Such fluid and tracers can raise the magnitude of weak anomalous signals
61from HAFZ to a detectable level. It is also proposed to use a steel-cased well as a boosting electric source
62that directly charges HAFZ (Schenkel and Morrison, 1994; Marsala et al., 2014; Commer et al., 2015;
63Hoversten et al., 2015; Um et al., 2015; Patzer et al., 2017). The sensitivity analysis of the approaches
64proposed above has been numerically carried out with simple inflated fracture geometries (Weiss et al.,
652016).

66 In this paper, we numerically evaluate a surface-based electrical method with a steel-cased well for
67detecting and imaging HAFZ. In our survey configuration, one end point of a surface electric dipole
68source is connected to the top of a steel-cased well to directly charge HAFZ around the well. The other

69point of the electric dipole source is grounded sufficiently away from the cased well. The electric fields
70are measured on the surface. For simplicity, we call this configuration the top-casing electric source
71method. The potential advantage of the method is to characterize HAFZ without requiring well
72intervention because both sources and receivers are placed on the surface. This advantage makes the
73proposed electrical method fast and economic in hydraulic fracturing operations and safe in hazardous
74waste disposal sites.

75 The remainder of this paper is organized as follows. First, we describe a 3D finite-element forward and
76inverse modeling algorithm for the electric resistivity method in the presence of a steel-cased well. To
77handle the multi-scale DC modeling associated with the presence of the steel-cased well, we introduce a
78dual-mesh-based algorithm that utilizes structured finite-difference (FD) imaging meshes and
79unstructured finite-element (FE) simulation meshes. The effectiveness of the dual-mesh approach for
80modeling a steel-cased well is discussed. Second, we present a simplified version of a steel-cased well
81model and show its accuracy and efficiency. Third, using the algorithms, we evaluate the detection
82sensitivity of the top-casing electrical source method for several simple 3D HAFZ. Finally, we show the
83imaging sensitivity of the method through inversion experiments as the final proof-of-concept analysis
84step.

85 FORWARD MODELING OF 3D ELECTRICAL RESISTIVITY METHOD

86 In this paper, we employ a 3D FE electrical resistivity modeling algorithm described in Um et al.
87(2010). The governing equation of the electric resistivity method is given as Poisson's equation

$$\nabla \times (\sigma(\mathbf{r}) \nabla \phi(\mathbf{r})) = -\nabla \cdot \mathbf{j}_s(\mathbf{r}), \quad (1)$$

88where $\phi(\mathbf{r})$ is a potential at position \mathbf{r} , $\sigma(\mathbf{r})$ is electrical conductivity, and \mathbf{j}_s is an electric source.

89 We discretize the computational domain with tetrahedral meshes. To develop the weak statement,
 90 equation 1 is multiplied by a weighting function $\omega(\mathbf{r})$ and is integrated over the volume of a tetrahedral
 91 element, resulting in

$$\iiint_{V^e} \omega^e(\mathbf{r}) \nabla \times (\sigma^e(\mathbf{r}) \nabla \phi^e(\mathbf{r}) + \nabla \phi_s^e(\mathbf{r})) dv = \Theta, \quad (2)$$

92 The superscript e indicates the e^{th} tetrahedral element. V^e is the volume of the e^{th} tetrahedral element.

93 The unknown potential at \mathbf{r} inside the e^{th} element is interpolated using the set of four Lagrange

94 polynomials $n_i^e(\mathbf{r})$ (Jin, 2015)

$$\phi^e(\mathbf{r}) = \sum_{i=1}^4 \phi_i^e n_i^e(\mathbf{r}), \quad (3)$$

95 where ϕ_i^e is the potential at the i^{th} node of the e^{th} element.

96 We also use the same Lagrange polynomials as the weighting function $\omega(\mathbf{r})$ in equation 3. Thus,

97 substituting equation 3 into equation 2 and replacing $\omega(\mathbf{r})$ by $n_i^e(\mathbf{r})$ result in

$$\mathbf{M}^e \mathbf{u}^e = \mathbf{s}^e \quad (4)$$

98, where

$$\mathbf{M}_{ij}^e = \iiint_{V^e} \sigma^e(\mathbf{r}) \left(\frac{\partial n_i^e}{\partial x} \frac{\partial n_j^e}{\partial x} + \frac{\partial n_i^e}{\partial y} \frac{\partial n_j^e}{\partial y} + \frac{\partial n_i^e}{\partial z} \frac{\partial n_j^e}{\partial z} \right) dV, \quad (5)$$

$$i \text{ element of } \mathbf{u}^e = [\phi_1^e \quad \phi_2^e \quad \phi_3^e \quad \phi_4^e], \quad (6)$$

$$i \text{ element of } \mathbf{s}^e = \iiint_{V^e} n_i^e(\mathbf{r}) \nabla \times \mathbf{j}_s(\mathbf{r}) dv, \quad (7)$$

99 Equation 4 is considered local because it comes from each tetrahedral element. Using the node
 100 connectivity information, local matrix equations from individual elements are assembled into a single
 101 global matrix equation.

102 The resulting system of FE equations is symmetric positive definite. Note that the system matrix is
 103 typically ill-conditioned because the contrast in conductivity across the air-casing interface can be larger
 104 than ten orders of magnitude and also because the discretization of a hollow cased well in a deep earth
 105 model requires mixing millimeter-scale elements with kilometer-scale ones (Um et al., 2015). Our choice
 106 of numerical linear algebra for equation 4 is sparse Cholesky factorization and subsequent backward and
 107 forward substitution (Davis, 2006). After the total potential is determined at each tetrahedral node, the
 108 potential difference at two arbitrary end-points of a finite-long electric dipole receiver is interpolated and
 109 divided by the length of the receiver.

110 INVERSE MODELING ALGORITHM WITH STEEL-CASED WELL

111 Our inversion implementation described here is based on a general frequency-domain EM inversion
 112 framework. An objective functional is given as

$$\Phi = [\mathbf{D}(\mathbf{d}_{\text{obs}} - \mathbf{d}_{\text{pred}})]^T [\mathbf{D}(\mathbf{d}_{\text{obs}} - \mathbf{d}_{\text{pred}})] + \lambda (\mathbf{W}\boldsymbol{\sigma})^T (\mathbf{W}\boldsymbol{\sigma}), \quad (8)$$

113 where \mathbf{D} is a data weighting matrix, \mathbf{d}_{obs} and \mathbf{d}_{pred} are observed and predicted DC data, respectively, \mathbf{W} is
 114 a regularization matrix defined by FD approximation to Laplacian operator, and $\boldsymbol{\sigma}$ is a conductivity
 115 model. λ is a regularization parameter.

116 Our inversion algorithm employs a limited-memory Broyden–Fletcher–Goldfarb–Shanno (L-BFGS)
 117 algorithm (Nocedal and Wright, 2006). Inside L-BFGS, a Cholesky factor for equation 4 is re-used to
 118 compute a search direction vector. Accordingly, one inversion iteration requires only one new
 119 factorization if the initial trial step satisfies sufficient decrease of Φ . If the trial step fails to sufficiently
 120 decrease Φ , a line search algorithm performs back-tracking. When multiple sources are used, they share

121the factored matrices. To prevent conductivity overshoots in the course of inversion, the conductivity
122model is bounded by a logarithmic transformation function (Newman and Alumbaugh, 2000).

123 To accurately and efficiently model a steel-cased well, our inversion scheme includes three
124characteristics. First, we use different meshes in the model and simulation domain. Note that dual mesh
125approaches have been widely used in EM imaging (Commer and Newman, 2008, Egbert and Kelbert,
1262012; Yang et al., 2014; Grayver, 2015; Yang et al., 2016). However, our dual mesh approach is distinct
127from others since we use a dual mesh approach with heterogeneous mesh types. Coarse rectangular FD
128meshes are used to define the model space (i.e. FD model meshes), whereas fine tetrahedral FE meshes
129(i.e. FE simulation meshes) are used to compute forward solutions and subsequent gradient vectors. The
130motivation behind the FE-FD dual mesh approach is multifold. First, by using the tetrahedral FE
131simulation meshes, the simulation domain is highly refined inside and around wells but remains coarse
132elsewhere, leading to efficient forward modeling in the presence of wells (Um et al., 2015). This is a
133prime advantage of our FE-FD dual mesh approach over a traditional FD-FD dual mesh approach where
134local refinements in simulation meshes extend both horizontally and vertically. Second, it is practical to
135use rectangular FD meshes in the model domain. For example, visualization and analysis of tetrahedral
136meshes are cumbersome and daunting especially when millimeter scale elements for wells are mixed with
137kilometer scale elements for regional geology. Rapid and accurate display of large multi-scale tetrahedral
138meshes is currently an active research area in both earth sciences and computer sciences. In contrast, the
139use of the structured FD model domain allows us to easily and rapidly visualize and analyze EM imaging
140results even in the course of inversion. This is a major practical advantage of our FE-FD dual mesh
141approach over single mesh FE inversion approaches and FD-FD approaches.

142 Second, we define two mapping matrices that connect one meshes with the other meshes: $\mathbf{M}_{\text{FE}2\text{FD}}$ and
143 $\mathbf{M}_{\text{FD}2\text{FE}}$ (Um et al., 2017). $\mathbf{M}_{\text{FD}2\text{FE}}$ is N_{FE} -by- N_{FD} , where N_{FD} and N_{FE} are the number of cells in the FD
144meshes and the number of tetrahedra in the FE meshes, respectively. Its (i,j) element is a ratio of an
145intersectional volume of the i^{th} FE element and the j^{th} FD cell to the volume of the i^{th} FE element. In

146contrast, $\mathbf{M}_{\text{FE2FD}}$ is a reverse operator of $\mathbf{M}_{\text{FD2FE}}$. Its size is N_{FD} -by- N_{FE} . Its (i,j) element is a ratio of an
147intersectional volume of the i^{th} FD cell and the j^{th} FE element to the volume of the i^{th} FD cell. Therefore,
148 $\mathbf{M}_{\text{FD2FE}}$ and $\mathbf{M}_{\text{FE2FD}}$ map σ from FD to FE and from FD to FE, respectively, being able to use
149heterogeneous mesh types in the model and simulation domain. More details on the two mapping
150matrices can be found in Appendix.

151 Third, after L-BFGS computes a search direction vector, $\mathbf{M}_{\text{FE2FD}}$ maps the vector from FE to FD. Before
152it is mapped to FD, its elements that correspond to the steel-cased wells are zeroed. The L-BFGS line
153search is performed in the FD model space to find a next conductivity model that decreases Φ . When a
154candidate FD model with a trial step length is formed, $\mathbf{M}_{\text{FD2FE}}$ maps the FD model to the FE simulation
155meshes. Note that the resulting FE model does not yet include the steel-cased well because the FD model
156in the model space does not include it. Therefore, at this point, the conductivity of the steel-cased well is
157assigned to the FE elements. Accordingly, the FD model space does not have fine grids for the steel-cased
158well but remains coarse, which is important for stable electrical resistivity imaging with a limited number
159of electrode receivers. In contrast, the FE modeling uses fine meshes, includes the steel-cased well, and
160accurately simulates EM responses to the wells. The implementation steps for our inversion are
161summarized below.

162 (1) Choose a starting FD/FE model.

163 (2) If it is a FD model, map it from FD to FE space using $\mathbf{M}_{\text{FD2FE}}$ and add prescribed cased wells to the
164FE model.

165 (3) Perform forward modeling and gradient calculation for the current model in the FE space by solving
166 equation 4.

167 Repeat:

168 (4) L-BFGS determines a search direction vector.

169 (5) Set elements of the vector that correspond to the cased well to zero.

170 (6) Map the vector from FE to FD space using $\mathbf{M}_{\text{FE2FD}}$.

171 Repeat:

172 (7) Create a candidate FD model with a trial step length.

173 (8) Map the candidate model from FD to FE using $\mathbf{M}_{\text{FD2FE}}$ and add the cased well to FE.

174 (9) Perform forward modeling and gradient calculation for the candidate model in the FE space.

175 (10) If Φ does not sufficiently decrease, choose a new trial step length.

176 Until Φ sufficiently decreases

177 Until stop criteria for inversion are met

178 **MODELING OF TOP-CASING ELECTRIC SOURCE METHOD**

179 The FE forward modeling algorithm with a direct solver has been proven accurate for computing
180 electric and EM responses to an earth model that features small-scale geometry and extreme conductivity
181 contrast of a steel-cased well (Commer et al., 2015; Um et al., 2015). Fine tetrahedral meshes are used to
182 accurately discretize arbitrarily complex fracture and well geometries and coarse meshes elsewhere.
183 However, the direct discretization of multiple long (e.g. a few kilometers) hollow cased wells requires a
184 number of tiny elements (e.g. a few ten million unknowns). Thus, modeling complex well structures with
185 direct solvers is often prohibitively expensive. In most cases, the direct FE discretization is useful for
186 generating reference responses to a cased well but is not practical enough for inverse modeling where a
187 number of forward modeling needs to be completed.

188 To practically model a steel-cased well in the 3D Cartesian coordinate system, several approximation
189 approaches have recently been proposed. For example, a hollow well can be approximated with a prism

190(Weiss et al., 2015; Puzyrev et al., 2016). Its conductivity value is determined such that the cross-
191sectional conductance of the prism is kept same as the hollow well. The well can also be replaced with a
192series of small electric dipoles along the well in the DC and frequency domain (Cuevas, 2014;
193Nieuwenhuis et al., 2015). Weiss (2017) introduces a hierarchical electrical conductivity model for
194representing complex steel infrastructures and fractures at low computational cost. The accuracy of the
195approximation methods depends on various factors including background geology, source types and
196frequencies, well completion designs and distribution, distances between wells, sources and receivers and
197others. Therefore, one needs to use an approximation method in its scope and compare approximate
198solutions with reference solutions.

199 Of the approximation methods above, our choice is to replace a hollow steel-cased well by a prism.
200Before we present detection and imaging sensitivity of the top-casing electric source method to HAFZ in
201the next sections, we first show its accuracy and effectiveness in the scope of our modeling problem. As
202shown in **Figure 1**, the size of a prism is set to the outer diameter of the casing. We use the mesh-
203generating software, TetGen (Si, 2015) to generate tetrahedral meshes. **Figure 2** shows that the two
204models produce nearly identical responses. The relative differences between the hollow steel-cased well
205and the prism rapidly decrease with increasing distance from the wells. This indicates that the detailed
206geometry of the well's outer surface becomes less important as a receiver position becomes distant from
207the well. After the replacement, the number of elements reduces from 8,421,559 to 745,151 elements,
208showing the effective reduction in modeling problem size without affecting the solution accuracy.
209Equation 4 for the model shown in **Figure 1b** is solved in about 3 minutes using 3.40GHz Intel Skylake
210processor, which is fast enough for forward and inverse modeling experiments in the next section.

211 In the next example, we consider a 1km long hollow steel-cased well and its corresponding cylinder and
212prisms. For independent verification, we compute surface electric DC responses with a Poisson solver
213that is embedded into the 3D FD time-domain modeling algorithm (Commer and Newman, 2004;
214Commer et al., 2015). Because FD and FE algorithms are different numerical solution approaches for the

215same physics, the agreement between FE and FD solutions will show not only the accuracy of our FE
216algorithm but also the validity of the prism approximation.

217 **Figure 3** shows a cross-sectional view of 1) a 1km long hollow steel-cased well, 2) its corresponding
218solid cylinder and 3) rectangular prism. One end point of an 870m long electric dipole source is
219connected with the surface of the steel-cased well and its alternatives. The background conductivity is set
220to 0.0333 S/m. Their surface electric field responses are shown in **Figure 4a**. Their relative differences
221with respect to the hollow well model are plotted in **Figure 4b**. For comparison, we also compute the
222electric field responses to the rectangular prism model using the FE algorithm described in this
223manuscript. The resulting FD and FE solutions agree well with each other. For example, the hollow steel-
224cased well and the solid cylinder (both FD models) produce nearly identical responses. When the steel-
225cased well is replaced with the rectangular prism, some numerical errors are introduced, but they are
226sufficiently small (less than 1.5%). The relative differences between the hollow steel-cased well model
227and its FD cylinder and prism models decrease with increasing distance from the well. The FE solution to
228the rectangular prism also agrees well with the three FD solutions, showing both the accuracy of the FE
229modeling algorithm and the validity of the casing approximation approach in the scope of our modeling
230problem.

231**FORWARD SENSITIVITY OF TOP-CASING ELECTRIC SOURCE METHOD TO HAFZ**

232 **Figure 5** shows a top-casing electric source configuration used in this study where one end point of the
233electric source is directly connected to the well head and the other end point is grounded sufficiently
234distant (2km) from the well head. A 2km long array of x -oriented electric receivers is placed along the $+x$
235direction at $y=0$ m (survey line 1) and a 4km long array of y -oriented electric receivers along the $\pm y$
236direction at $x=2$ km (survey line 2). We consider an L-shaped well for simplicity. The vertical part of the
237well is 1.6 km deep and the horizontal part 400 m long. The casing is $5 \cdot 10^6$ (S/m) conductive and its
238diameter is set to 0.3 m. The well is replaced to its equivalent rectangular prism discussed earlier.

239 Because of the high contrast of electrical conductivity between the prism and the background geology,
240the high concentration of the electrical current preferentially flows along the surface of the prism and
241directly charges HAFZ. We consider that the high-pressure injection of saline fluid creates HAFZ (Kim et
242al., 2014). HAFZ is created perpendicular to the horizontal well and 200m away from the vertical well.
243Note that this is a relatively shallow hydraulic fracturing model. Depths of fracturing operations range
244from 3 to 5 km (Fisher and Warpinski, 2012). Their lateral distance from the vertical well also varies from
2451.6 to 5km. The deeper depth and longer lateral distance mean that anomalous responses to HAFZ can be
246significantly smaller than those shown here. Accordingly, they would be vulnerable to cultural noises. In
247such cases, one may need to consider downhole based methods presented in Hoversten et al. (2017).
248While we are aware of the challenging issues associated with deep fracturing problems, here we mostly
249focus on the relatively shallow problem as the basic feasibility study of the top-casing source electric
250method.

251 **Figure 6** shows simple four HAFZ models considered in this study. Their dimensions are summarized
252in **Table 1**. Note that the fracture propagation is bounded within the overburden and underburden layers
253that have higher minimum horizontal stress and/or higher strength than those of the reservoir, propagating
254in a horizontal direction. The size and the shape of the HAFZ models above are comparable to those that
255can be determined by well-known analytic fracture models such as Khristianovic-Geertsma-de Klerk
256(KGD) and Perkins-Kern-Nordgen (PKN) fracture (Perkins and Kern, 1961; Geertsma and de Klerk,
2571969; Nordgren, 1972; Daneshy, 1973; Gidley et al., 1990) and thus, honor basic geomechanics
258associated with fractures. As shown in **Table 1**, we do not consider directly modeling micro-scale fracture
259networks. Rather, the thickness of the fracture networks is artificially inflated into 1m thick HAFZ in a
260volume-averaged sense as done in Weiss et al. (2015) and Hoversten et al. (2017). The inflation approach
261is geophysically reasonable when the low resolution of the electrical method and the distance between
262source/receiver and HAFZ are considered.

263 Before we present numerical modeling examples, we briefly discuss a noise floor. In active fracturing
264 sites and oil fields, the noise floor may vary by several orders of magnitude. For example, Tietze et al.
265 (2015) report that the noise floor of electric field measurements in a German oil field is about 10^{-10} V/m,
266 which is subsequently considered a noise floor in Hoversten et al. (2107). It is also reported that the floor
267 can often be close to 10^{-7} V/m. Therefore, to achieve a desired noise floor in practice, one must consider
268 stacking data. For example, when the raw noise floor is 10^{-9} to 10^{-7} V/m, 100 to 1,000,000 stacking
269 operations are required to achieve 10^{-10} V/m noise floor.

270 **Figure 7** shows the electrical field measurements along survey line 1 and 2 over the four HAFZ
271 models. The top-casing electrical source method clearly distinguishes between the four models. Their
272 electric field amplitudes are larger than both optimistic and pessimistic noise floors discussed earlier. To
273 highlight the role of the steel-cased well as a conduit for a high concentration of electric currents that
274 charge HAFZ, we repeat the same modeling without the casing. **Figure 8** shows that the electrical field
275 measurements over the background model and the four models are nearly identical. The surface electrical
276 method does not sense the presence of HAFZ. This modeling shows that steel-cased wells that have been
277 regarded as a disturbance to electrical and EM geophysics can be beneficial for sensing deep localized
278 targets when the wells responses can be accurately and efficiently modeled.

279 Next, we examine two factors that directly control the sensitivity of the electrical method to HAFZ. The
280 first factor is the continuity of the steel cased well. **Figure 9** shows the electric field measurements over
281 three different continuity conditions: the intact casing, the corroded casing and the broken casing. To
282 realize a corroded casing condition, we consider a 1m long low conductivity patch ($5 \cdot 10^{-3}$ S/m) at $z=500$ m.
283 When the casing is completely broken, the 1m long patch has the conductivity of the background ($5 \cdot 10^{-3}$
284 S/m). As the continuity is deteriorated due to the corrosion, the method still distinguishes between the
285 four HAFZ models but its sensitivity decreases. The complete break no longer allows the high
286 concentration of electrical currents to efficiently flow along the casing and charge HAFZ, resulting in the
287 complete loss of the sensitivity.

288 The conductivity of the background geology also plays an important role in controlling the overall
289 sensitivity of the method. **Figure 10** shows the electric field measurement along survey line 1 with three
290 different background conductivities ranging from $5 \cdot 10^{-2}$ S/m to $5 \cdot 10^{-1}$ S/m. As the background geology
291 becomes more conductive, the sensitivity sharply decreases. The loss of the sensitivity is explained by the
292 fact that in more conductive background, casing tends to leak more currents horizontally and limits the
293 flow of the currents to HAFZ. In general, the top-casing electrical source method may not work well in
294 highly conductive earth environments. However, we have found that the presence of oil-based mud has
295 potential to improve the sensitivity of the top-casing electric source method even in a conductive
296 environment, because the mud is highly resistive up to 1,000 Ohm-m and reduces leaking current from
297 the well (Jannin et al., 2018). To examine the effect of the oil-based mud on the sensitivity, we assume
298 that the L-shaped well (**Figure 5**) is coated with 0.2m thick, 100 Ohm-m oil-based mud and compute the
299 surface electric field responses to the fractures in two conductive ($5 \cdot 10^{-2}$ and $5 \cdot 10^{-1}$ S/m) background
300 models (**Figure 11**). The comparison of **Figures 10** and **11** shows that the presence of thin oil-based mud
301 coating increases the sensitivity of the method by about 80%, demonstrating the potential benefit of oil-
302 based mud for the top-casing source method for detecting deep HAFZ in a conductive environment.

303 INVERSE SENSITIVITY OF TOP-CASING ELECTRIC SOURCE METHOD TO HAFZ

304 In this section, we examine the imaging sensitivity to the four HAFZ models (**Figure 6** and **Table 1**) as
305 the final step of proof-of-concept studies for the top-casing electrical source method. To ensure the
306 detection sensitivity to HAFZ, we assume that the background geology is resistive enough (i.e. $5 \cdot 10^{-3}$
307 S/m) such that the electrical currents can flow through the casing without significant leakage. The
308 Permian Basin and the Marcellus shale can be considered such resistive. We also assume that the cased
309 well is homogeneous and continuous. In addition, we adapt two extra assumptions from Hoversten et al.
310 (2017) that (1) electric field measurements are contaminated with 1% error of their amplitudes and (2)
311 electric field noise floor is 10^{-10} V/m. The four assumptions might not always be satisfied in practice.

312 However, the consideration about their potential influences is avoided in this study to focus on the basic
313 imaging capabilities of the top-casing electrical methods for HAFZ.

314 **Figure 12** summarizes the imaging experiment over HAFZ model 1. The starting model is a $5 \cdot 10^{-3}$ S/m
315 homogeneous half-space. An imaging domain covers $0 \leq x \leq 400$, $-1000 \leq y \leq 1000$ and $1000 \leq z \leq 2000$ m. In
316 other words, we assume that HAFZ resides inside the volume defined by the imaging domain. The L-
317 BFGS-based imaging algorithm implemented here work well and converges after 15 iterations. The
318 inversion is completed in 3 hours on 3.40GHz Intel Skylake processor with 64 GB memory. After the
319 convergence, both observed and predicted data show good agreements. The inversion reasonably recovers
320 the overall geometry of the HAFZ model 1 on the yz plane at $x=200$ m (**Figure 12a**) although some
321 scattered artifacts are seen on the xz plane at $y=0$ m (**Figure 12b**).

322 Note that the boundaries of the recovered HAFZ are not smooth but somewhat irregular. This is because
323 we use a relatively small regularization parameter in our inversion. A proper small regularization
324 parameter is empirically determined via trial errors. It is our experience that a traditional cooling method
325 with a large starting regularization parameter often smooths out a thin HAFZ structure in early inversion
326 stages and fails to recover the fracture geometry in late stages with a small parameter. Accordingly,
327 choosing a small starting regularization parameter is our practical choice for imaging thin HAFZ when a
328 smooth background conductivity model is determined by other geophysical methods (e.g. Um et al.,
329 2014).

330 In the experiment above, our imaging domain does not cover the entire modeling volume. We have
331 found out that such a large imaging domain often leads to non-geological imaging results (e.g. highly
332 scattered conductive structures). Instead, our imaging domain covers the horizontal well area with
333 sufficient room for fracture developments in both lateral and vertical direction. While our proof-of-
334 concept studies assume that the HAFZ is perpendicular to the well, realistic scenarios may involve that its
335 geometry changes over time. Therefore, 400-by-2000-by1000m volume of the imaging domain would be

336reasonable. However, knowledge of both the fluid injection location and the amount of the injected fluid
337helps us to estimate a possible maximum volume of the imaging domain (Hoversten et al., 2017).
338Coupled flow and geomechanics simulation for various scenarios with different geological media (Kim
339and Moridis, 2013) can further assist refining the imaging domain size.

340 MEQ analysis can also roughly tell us about the locations of fracturing events, helping us better define a
341volume of the imaging domain. Therefore, it is worth to perform imaging experiments with an MEQ-
342guided imaging domain. For example, we assume that by having MEQ analysis, we can reduce $0 \leq x \leq 400$
343of the imaging domain to $175 \leq x \leq 225$ m where we have an injection point at ($x=200$ m, $y=0$ m and
344 $z=1600$ m). The assumption is also reasonable from geomechanical perspectives because the domain size
345of 50m in the x direction would be sufficiently large such that HAFZ can contain both main fracture
346networks and small micro-fractures/fissures that can induce substantial leakage of injection fluid (Fisher
347and Warpinski, 2012). The other dimensions of the imaging domain keep the same as those used in
348**Figure 12**.

349 **Figure 13** shows the imaging experiments for model 1 with the imaging domain constrained in the x
350direction. Although the thickness of HAFZ model 1 is still not clearly resolved but blurred, the width and
351the height of model 1 are slightly better resolved. The use of the tight imaging domain also prevents
352unrealistic scattered conductive structures on the xz plane at $y=0$ m shown in **Figure 12b**. **Figures 14-16**
353show the imaging experiments for the remaining three HAFZ models with the same constrained imaging
354domain. **Figures 13-16** clearly show that the casing-top electrical method can effectively delineate
355systematical changes in the width and the height of HAFZ although it is still daunting to resolve the
356thickness even in the imaging domain constrained in its direction.

357 Our last inversion experiment examines the effects of a higher noise level on the imaging sensitivity. To
358do this, the noise level for model 1 increases from 1 to 5 %. All other inverse modeling parameters and
359the volume of the imaging domain keep the same as those used in **Figure 13**. **Figure 17** summarizes the

360 imaging experiment with the high noise level. The inversion algorithm performs well and its convergence
361 is similar to the previous examples. Compared with the inversion result with 1% noise (**Figure 13**), the
362 height of HAFZ is reasonably recovered, but the accuracy of the width is deteriorated. This inversion
363 example illustrates the importance of data quality for accurately resolving the detailed geometry of
364 HAFZ.

365 CONCLUSION

366 We have presented advanced 3D electrical resistivity modeling and imaging algorithms that utilize
367 heterogeneous types of meshes. The coarse rectangular FD meshes are used in the imaging domain to
368 facilitate visualization and analysis of imaging results, whereas the tetrahedral FE simulation meshes are
369 used for efficiently and accurately discretizing a multi-scale earth model. Linear mapping operators based
370 on volume-averaging provides a robust link between the two difference mesh topologies. The algorithms
371 are well suited to modeling and inverting electric field measurements in the presence of a steel-cased
372 well. We have shown that a steel-cased well can be replaced by a prism. This replacement reduces the
373 computational cost without deteriorating the solution accuracy, making it possible to rapidly simulate
374 electric field responses over a 3D earth model in the presence of a steel-cased well.

375 We have shown that the top-casing electrical method is sensitive to and can delineate a localized HAFZ
376 in a shallow depth. The primary advantage of the proposed method is the fact that the method employs
377 surface sources and receivers and thus does not require borehole occupancy and interruption to the normal
378 operation of the wells. As a result, its data acquisition can be cheaper and less cumbersome. We have
379 numerically shown that the top-casing electric source method has potential to image HAFZ. The imaging
380 results can be improved if the imaging domain is constrained.

381 To evaluate the proof of concept for the top-casing electrical method, our feasibility studies focused on
382 fairly simple 3D HAFZ models. Several assumptions were also made to render our studies simple. For
383 example, HAFZ is relatively shallow. The properties of the background geology and the steel-cased well

384 were assumed known. However, in practice, it may not be always straightforward to characterize a deep
385 localized HAFZ. A baseline resistivity model should be determined before hydraulic fracturing
386 operations. The casing properties are also often unknown and may need to be determined by inversion.
387 Accordingly, we expect that there are still challenges to accurately characterize deep HAFZ in practice.
388 However, the feasibility studies presented here is encouraging. When the top-casing source method is
389 considered for imaging HAFZ, the challenges described above will be important research topics.

390 **ACKNOWLEDGEMENT**

391

392 **APPENDIX. MAPPING MATRICES $\mathbf{M}_{\text{FE2FD}}$ and $\mathbf{M}_{\text{FD2FE}}$**

393 The mapping processes from FD to FE meshes are casted into

$$\boldsymbol{\sigma}^{FE} = \mathbf{M}_{\text{FD2FE}} \boldsymbol{\sigma}^{FD}; \quad (\text{A1})$$

$$\mathbf{M}_{\text{FD2FE}ij} = \frac{1}{v_i^{FE}} \times (v_i^{FE} \cap v_j^{FD}) \quad (\text{A2})$$

(i,j) element of

394 N_{FE} -by- N_{FD} matrix $\mathbf{M}_{\text{FD2FE}}$ is a mapping operator from FD to FE meshes. Vectors $\boldsymbol{\sigma}^{FE}$ and $\boldsymbol{\sigma}^{FD}$ contain

395 conductivity attributes of the FE and FD models, respectively. v_i^{FE} and v_j^{FD} are the volume of the i^{th} FE

396 element and the j^{th} FD element, respectively. The intersection operator \cap computes the overlapping

397 volume of the FE and FD cell if they intersect.

398 N_{FD} -by- N_{FE} matrix $\mathbf{M}_{\text{FE2FD}}$ is defined in the reverse way as shown below.

$$\boldsymbol{\sigma}^{FD} = \mathbf{M}_{\text{FE2FD}} \boldsymbol{\sigma}^{FE}; \quad (\text{A3})$$

$$\mathbf{M}_{\text{FE2FD}ij} = \frac{1}{v_i^{FD}} \times (v_i^{FD} \cap v_j^{FE}) \quad (\text{A4})$$

(i,j) element of

399

400REFERENCES

- 401 Jannin, G., J. Chen, L. DePavia, L. Sun and M. Schwart, 2017, Deep electrode: A game-changing
402technology for electromagnetic (EM) telemetry, Annual International Meeting, SEG, Expanded Abstracts,
4031059-1062.
- 404 Commer, M., G. M. Hoversten, and E. S. Um, 2015, Transient-electromagnetic finite-difference time-
405domain earth modeling over steel infrastructure, *Geophysics*, **80**, E147-E162.
- 406 Commer, M., and G. A. Newman, 2008, New advances in three-dimensional controlled-source
407electromagnetic inversion, *Geophysical Journal International*, **172**, 513-535.
- 408 Commer, M. and G. A. Newman, 2004, A parallel finite-difference approach for 3D transient
409electromagnetic modeling with galvanic sources, *Geophysics* **69**, 1192-1202.
- 410 Cuevas, N., 2014, Analytical solutions of EM fields due to a dipole source inside an infinite casing,
411*Geophysics*, 79, E231-241.
- 412 Daneshy, A.A., 1973. On the Design of Vertical Hydraulic Fractures. *SPE Journal of Petroleum*
413*Technology* **25**, 83-97.
- 414 Davis, T.A., 2006, Direct methods for sparse linear systems, *Society for Industrial and Applied*
415*Mathematics*.
- 416 Egbert, G. D., and A. Kelbert, 2012, Computational recipes for electromagnetic inverse
417problems, *Geophysical Journal International*, **189**, 251-267.
- 418 Fisher, K., and N. Warpinski, 2012, Hydraulic fracture-height growth: real data. *SPE Prod. Oper.* **27**, 8-
41919
- 420 Grayver, A. V., 2015, Parallel three-dimensional magnetotelluric inversion using adaptive finite-element
421method. Part I: theory and synthetic study, *Geophysical Journal International*, **202**, 584-603.

422 Geertsma, J., and F. de Klerk, 1969. A Rapid Method of Predicting Width and Extent of Hydraulic
423Induced Fractures. *J Pet Technol* **2**, 1571-1581, SPE-2458-PA.

424 Gidley, J.L., S. A. Holditch, D. E. Nierode, W. Ralph, and R. W. Veatch, 1990, Recent advances in
425hydraulic fracturing. *SPE Monograph Series Vol. 12*.

426 Hoversten, G. M., Commer, M., E. Haber, and C. Schwarzbach, 2015, Hydro-frac monitoring using
427ground time-domain electromagnetics, *Geophysical Prospecting*, **63**, 1508-1526.

428 Hoversten, M., C. Schawrzbach, E. Haber, P. Belliveau and R. Shekhtman, 2017, Borehole to surface
429electromagnetic monitoring of hydraulic fractures, 6th International Symposium on Three-Dimensional
430Electromagnetics, Berkeley, California, USA.

431 Jin, J.M., 2015, *The finite element method in electromagnetics*, 3rd edition, John Wiley & Sons.

432 Johnston, R. and J. Shralow, 2011, Ambiguity in microseismic monitoring. *Annual International*
433Meeting, SEG, Expanded Abstracts, 1514-1518.

434 Kim, J. and G. J. Moridis, 2013, Development of the T+ M coupled flow–geomechanical simulator to
435describe fracture propagation and coupled flow–thermal–geomechanical processes in tight/shale gas
436systems. *Computers & Geosciences*, **60**, 184-198.

437 Kim, J., E. S. Um, and G. J. Moridis, 2014, Fracture propagation, fluid flow, and geomechanics of
438water-based hydraulic fracturing in shale gas systems and electromagnetic geophysical monitoring of
439fluid migration, *SPE Hydraulic Fracturing Technology Conference*, Society of Petroleum Engineers.

440 Marsala, A.F., A. D. Hibbs, and H. F. Morrison, 2014, December. Evaluation of Borehole Casing
441Sources for Electromagnetic Imaging of Deep Formations, *International Petroleum Technology*
442Conference.

443 Moridis, G.J. and C. M. Oldenburg, 2001, Process for guidance, containment, treatment, and imaging in
444a subsurface environment utilizing ferro-fluids (No. US 6250848), Lawrence Berkeley National
445Laboratory (LBNL), Berkeley, CA.

446 Newman, G.A. and D. L. Alumbaugh, 2000. Three-dimensional magnetotelluric inversion using non-
447linear conjugate gradients. *Geophysical journal international*, **140**, 410-424.

448 Nieuwemhuis, G., D. Yang, K. MacLennan, D. Oldenburg, M. Wilt and V. Ramadoss, 2015, Electrical
449imaging using a well casing as an antenna: a case study from a CO₂ sequestration site in Montana,
450American Geophysical Union Meeting.

451 Nocedal, J., and S. Wright, 2006, Numerical optimization, Springer Science & Business Media.

452 Nordgren, R.P., 1972. Propagation of a Vertical Hydraulic Fracture. *SPE J.* 12 (4): 306–314. SPE-3009-
453PA.

454 Patzer, C., K. Tietze, and O. Ritter, 2017, Steel-cased wells in 3-D controlled source EM
455modelling. *Geophysical Journal International*, **209**, 813-826.

456 Perkins, T.K., and L. R. Kern, 1961. Widths of Hydraulic Fractures. *J Pet Technol*, **13**, 937–949.

457 Puzyrev, V., E. Vilamajo, P. Queralt, J. Ledo, and A. Marcuello, 2016, Three-Dimensional Modeling of
458the Casing Effect in Onshore Controlled-Source Electromagnetic Surveys, *Surveys in Geophysics*, **38**,
459527-545.

460 Rahmani, A.R., A. E. Athey, J. Chen, and M. J. Wilt, 2014, Sensitivity of dipole magnetic tomography
461to magnetic nanoparticle injectates, *Journal of Applied Geophysics*, **103**, 199-214.

462 Schenkel, C.J. and H. F. Morrison, 1994. Electrical resistivity measurement through metal
463casing. *Geophysics*, **59**, 1072-1082.

464 Si, H., 2015, TetGen, a Delaunay-based quality tetrahedral mesh generator. ACM Transactions on
465Mathematical Software (TOMS), **4**, 11.

466 Tietze, K., O. Ritter, and P. Veeken, 2015, Controlled-source electromagnetic monitoring of reservoir
467oil saturation using a novel borehole-to-surface configuration, Geophysical Prospecting, **63**, 1468-1490.

468 Um, E. S., J. M. Harris, and D. L. Alumbaugh, 2010. 3D time-domain simulation of electromagnetic
469diffusion phenomena: A finite-element electric-field approach. Geophysics, **75**, F115-F126.

470 Um, E. S., M. Commer, and G. Newman. 2014, A strategy for coupled 3D imaging of large-scale
471seismic and electromagnetic data sets: Application to subsalt imaging, Geophysics **79**, ID1-ID13.

472 Um, E. S., M. Commer, G. A. Newman, and G. M. Hoversten, 2015. Finite element modelling of
473transient electromagnetic fields near steel-cased wells. Geophysical Journal International, **202**, 901-913.

474 Um, E. S., S. Kim and H. Fu, 2017, A tetrahedral mesh generation approach for 3D marine controlled-
475source electromagnetic modeling, Computer and Geosciences, **100**, 1-9.

476 Vermilyen, J.P. and M.D. Zoback. 2011. Hydraulic fracturing, microseismic magnitudes, and stress
477 evolution in the Barnett Shale, Texas, USA. SPE Hydraulic Fracturing Technology Conference, The
478 woodland, TX, 24 – 26 Jan. 2011.

479 Warpinski, N.R., R.C. Kramm, J.R. Heinze, and C.K. Waltman. 2005. Comparison of single- and dual-
480 array microseismic mapping techniques in the Barnett shale. SPE ATCE, Dallas, TX, Oct. 9 – 12 2005.

481 Weiss, C. J., D. F. Aldridge, H. A. Knox, K. A. Schramm, and L. C. Bartel, 2016, The direct-current
482response of electrically conducting fractures excited by a grounded current source. Geophysics, **81**, E201-
483E210.

484 Weiss, C., 2017, Finite-element analysis for model parameters distributed on a hierarchy of geometric
485simplices, Geophysics, **82**, no. 4, E155-E167.

486 Yang, D., D. Oldenburg, and E. Haber, 2014, 3-D inversion of airborne electromagnetic data
487parallelized and accelerated by local mesh and adaptive soundings: Geophysical Journal International,
488**196**, 1942-1507.

489 Yang, D., and D. Oldenburg, 2016, Survey decomposition: A scalable framework for 3D controlled-
490source electromagnetic inversion: Geophysics, **81**, E69-E87.

491 Zoback M.D. 2007 Reservoir geomechanics. Cambridge, Cambridge university press.

492 Zoback, M., Kitasei, S., and Copithorne, B. 2010 Addressing the environmental risks from shale gas
493development. World Watch Institute Briefing Paper 1, World watch Institute (Washington DC)

494 **FIGURE CAPTIONS**

495 **Figure 1.** (a) 200m long hollow steel-cased well model. The air, the earth and the casing are set to $3 \cdot 10^{-7}$, $3 \cdot 10^{-2}$ and 10^6 (S/m), respectively. (b) Its corresponding solid rectangular prism model.

497 **Figure 2.** Comparison of surface +x-oriented electric field responses to the two models (**Figure 1**).

498 **Figure 3.** XY cross-sectional views of 3D FD models with a conductivity color bar (log scale). (a) A 499 1km long vertical hollow steel-cased well. (b) A solid cylinder that has the same outer diameter of the 500 hollow steel-cased well. (c) A rectangular prism of which its side length is equal to the diameter of the 501 hollow steel-cased well. The earth and the casing are set to $3.33 \cdot 10^{-2}$ and $5 \cdot 10^6$ S/m, respectively. The 502 cylinder and prism are set to $1.73 \cdot 10^6$ and $1.36 \cdot 10^6$ S/m, respectively. R_{in} and R_{out} represent the inner and 503 outer radius of the casing, and W the width of the rectangular prism.

504 **Figure 4.** Comparison of DC responses to the true and approximate casing models shown in **Figure 3**. 505 (a) Surface +x-oriented electric field responses. (b) Relative differences of the approximate model 506 responses with respect to the hollow cased well model response.

507 **Figure 5.** A top-casing electric source configuration for detecting HAFZ at $z=1.6$ km and $x=200$ m. X- 508 oriented and y-oriented electric fields are measured along survey line 1 and 2, respectively.

509 **Figure 6.** The four hydraulically active fractured zone models. The yz cross-sectional view at $x=200$ m 510 (a) Model 1. (b) Model 2. (c) Model 3. (d) Model 4.

511 **Figure 7.** Electric field measurements along (a) survey line 1 and (b) survey line 2 and their relative 512 difference with respect to the 0.005 S/m (200 Ohm-m) background response.

513 **Figure 8.** Electric field measurements without the steel-cased well along (a) survey line 1 and (b) 514 survey line 2 and their relative difference with respect to the background response.

515 **Figure 9.** Electric field measurements along +x axis (survey line 1) with partially and fully damaged
516 cased wells. (a) Intact ($5 \cdot 10^6$ S/m) casing (**Figure 5a**). (b) The corroded ($5 \cdot 10^3$ S/m) casing at $z=500$ m. (c)
517 The completely broken casing at $z=500$ m.

518 **Figure 10.** Electric field measurements along +x axis (survey line 1) with different background
519 conductivity values. (a) Background conductivity= $5 \cdot 10^{-2}$ S/m. (b) Background conductivity= $5 \cdot 10^{-1}$ S/m.

520 **Figure 11.** Electric field measurements along +x axis (survey line 1) with different background
521 conductivity values. (a) Background conductivity= $5 \cdot 10^{-2}$ S/m. (b) Background conductivity= $5 \cdot 10^{-1}$ S/m.
522 The cased well is coated with 0.2m thick 10^{-2} S/m oil-based mud.

523 **Figure 12.** Inversion for model 1. (a) YZ cross-sectional view at $x=200$ m. (b) XZ cross-sectional view at
524 $y=0$ m. (c) Data plots along line 1 before and after the inversion. (d) Data plots along line 2 before and
525 after the inversion. (e) Misfit as a function of inversion iteration. The white boxes in (a) and (b) indicate
526 the true boundaries of model 1.

527 **Figure 13.** Inversion for model 1 with the imaging domain constrained in the x-direction. (a) YZ cross-
528 sectional view at $x=200$ m. (b) XZ cross-sectional view at $y=0$ m. (c) Data plots along line 1 before and
529 after the inversion. (d) Data plots along line 2 before and after the inversion. (e) Misfit as a function of
530 inversion iteration. The white boxes in (a) and (b) indicate the true boundaries of model 1.

531 **Figure 14.** Inversion for model 2 with the imaging domain constrained in the x-direction. (a) YZ cross-
532 sectional view at $x=200$ m. (b) XZ cross-sectional view at $y=0$ m. (c) Data plots along line 1 before and
533 after the inversion. (d) Data plots along line 2 before and after the inversion. (e) Misfit as a function of
534 inversion iteration. The white boxes in (a) and (b) indicate the true boundaries of model 2.

535 **Figure 15.** Inversion for model 3 with the imaging domain constrained in the x-direction. (a) YZ cross-
536 sectional view at $x=200$ m. (b) XZ cross-sectional view at $y=0$ m. (c) Data plots along line 1 before and

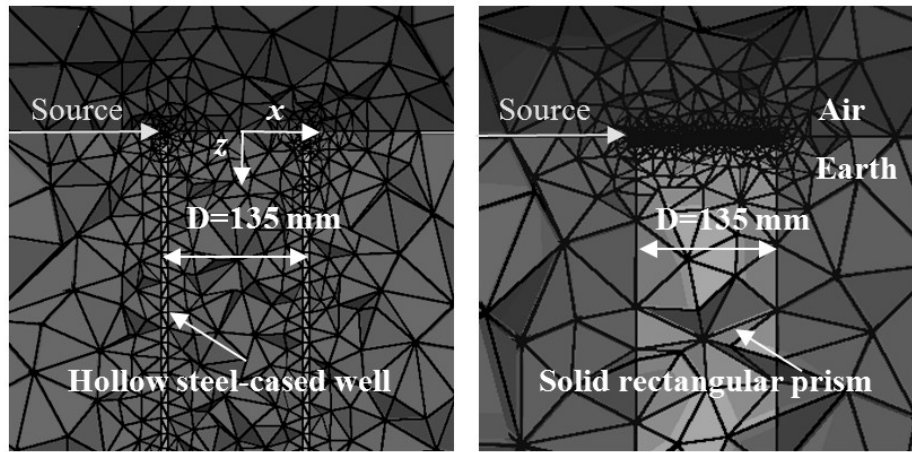
537after the inversion. (d) Data plots along line 2 before and after the inversion. (e) Misfit as a function of
538inversion iteration. The white boxes in (a) and (b) indicate the true boundaries of model 3.

539 **Figure 16.** Inversion for model 4 with the imaging domain constrained in the x-direction.. (a) YZ cross-
540sectional view at x=200m. (b) XZ cross-sectional view at y=0m. (c) Data plots along line 1 before and
541after the inversion. (d) Data plots along line 2 before and after the inversion. (e) Misfit as a function of
542inversion iteration. The white boxes in (a) and (b) indicate the true boundaries of model 4.

543 **Figure 17.** Inversion for model 1 with 5% noise level. (a) YZ cross-sectional view at x=200m. (b) XZ
544cross-sectional view at y=0m. (c) Data plots along line 1 before and after the inversion. (d) Data plots
545along line 2 before and after the inversion. (e) Misfit as a function of inversion iteration.

546

547 FIGURES



548

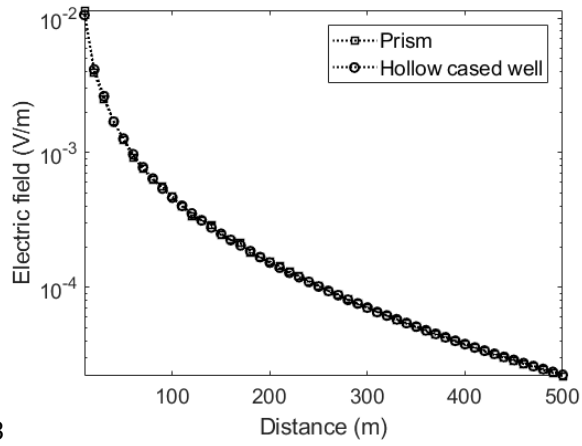
549

(a)

(b)

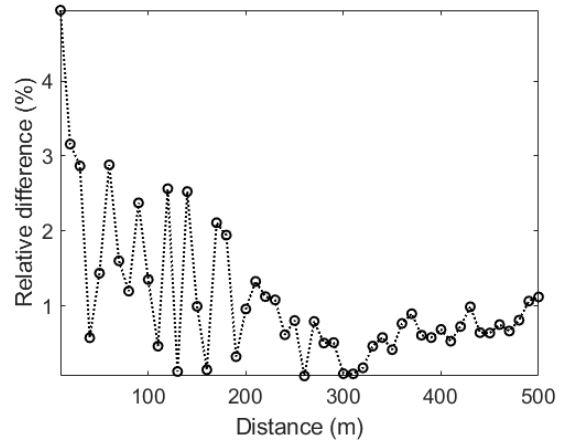
550 **Figure 1.** (a) 200m long hollow steel-cased well model. The air, the earth and the casing are set to $3 \cdot 10^{-7}$,
551 $13 \cdot 10^{-2}$ and 10^6 (S/m), respectively. (b) Its corresponding solid rectangular prism model.

552



553

(a)

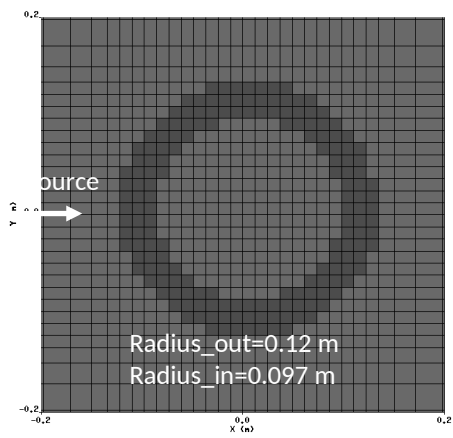


554

(b)

555 **Figure 2.** Comparison of surface +x-oriented electric field responses to the two models (**Figure 1**).

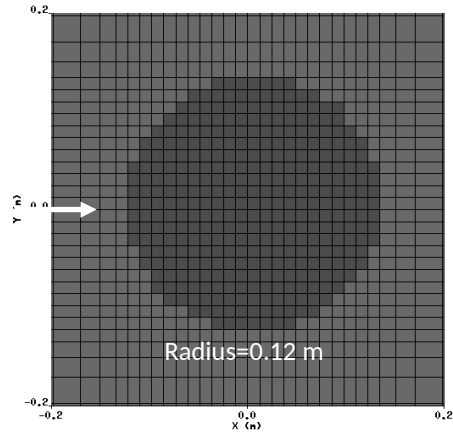
556



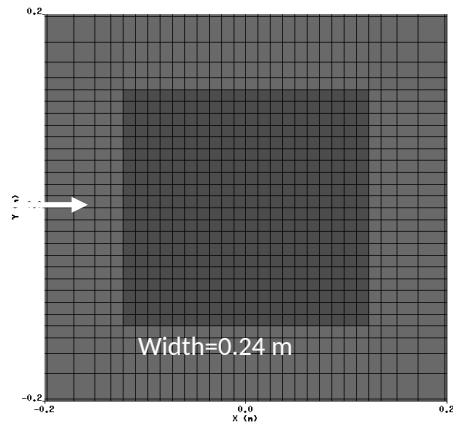
557

558

(a)



(b)



559

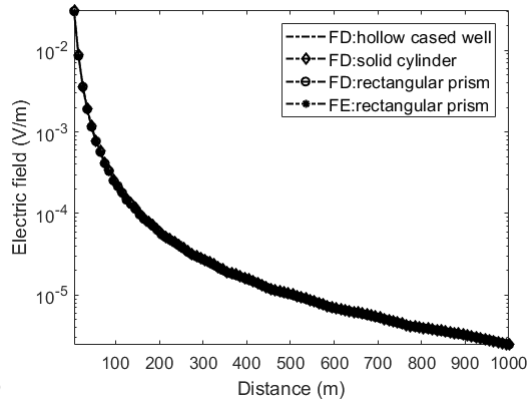
560

(c)

561 **Figure 3.** XY cross-sectional views of 3D FD models with a conductivity color bar (log scale). (a) A
 562 1km long vertical hollow steel-cased well. (b) A solid cylinder that has the same outer diameter of the
 563 hollow steel-cased well. (c) A rectangular prism of which its side length is equal to the diameter of the
 564 hollow steel-cased well. The earth and the casing are set to $3.33 \cdot 10^{-2}$ and $5 \cdot 10^6$ S/m, respectively. The
 565 cylinder and prism are set to $1.73 \cdot 10^6$ and $1.36 \cdot 10^6$ S/m, respectively. R_{in} and R_{out} represent the inner and
 566 outer radius of the casing, and W the width of the rectangular prism.

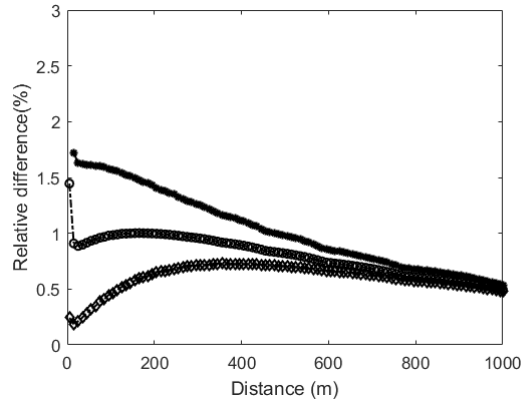
567

568



569

(a)

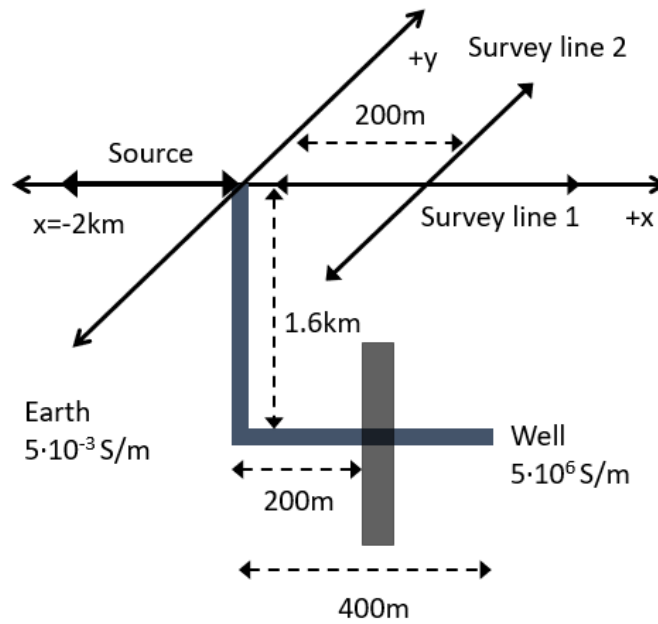


(b)

570

571 **Figure 4.** Comparison of DC responses to the true and approximate casing models shown in **Figure 3.** (a)
572 Surface +x-oriented electric field responses. (b) Relative differences of the approximate model responses
573 with respect to the hollow cased well model response.

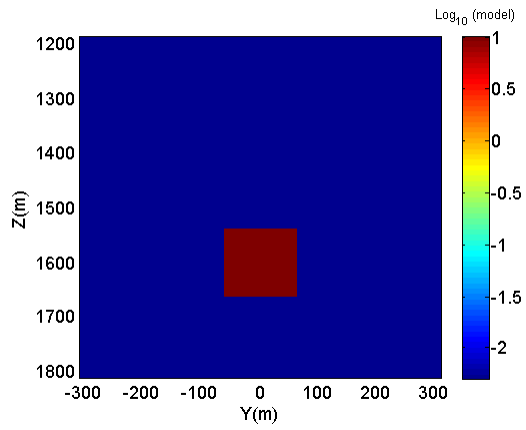
574



575

576 **Figure 5.** A top-casing electric source configuration for detecting HAFZ at $z = 1.6 \text{ km}$ and $x = 200 \text{ m}$. X -
577 oriented and y -oriented electric fields are measured along survey line 1 and 2, respectively.

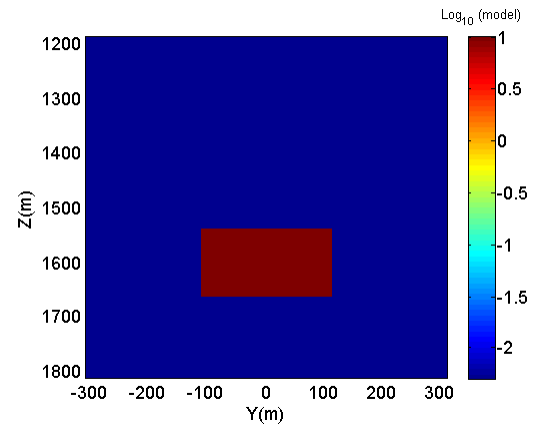
578



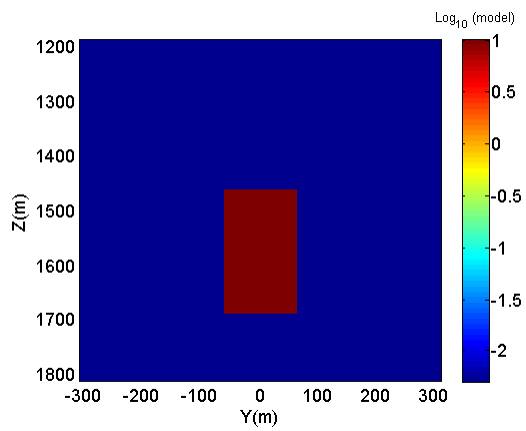
579

580

(a)



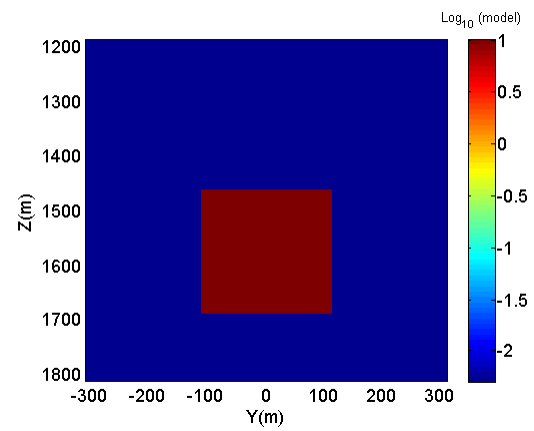
(b)



581

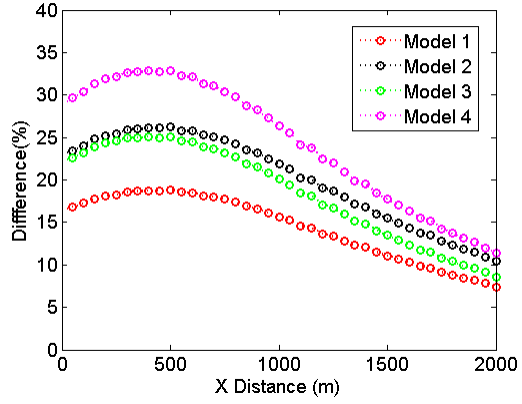
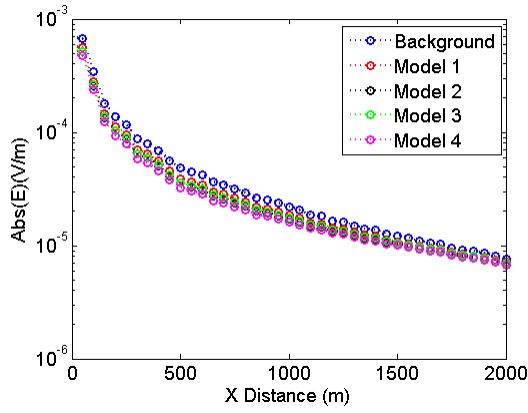
582

(c)



(d)

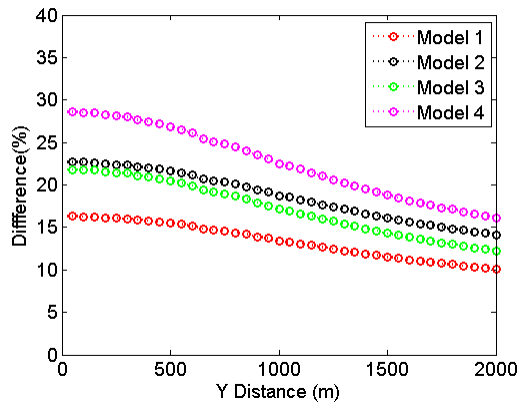
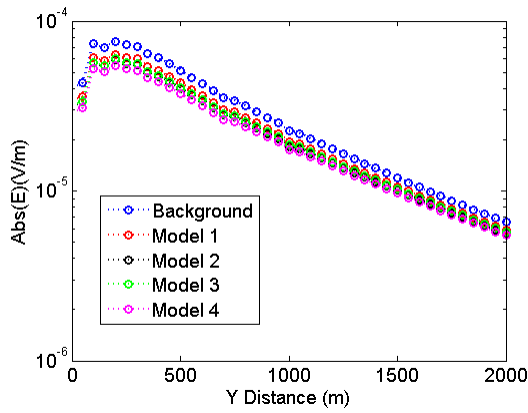
583 **Figure 6.** The four hydraulically active fractured zone models. The yz cross-sectional view at x=200m (a)
 584 Model 1. (b) Model 2. (c) Model 3. (d) Model 4.



585

586

(a)



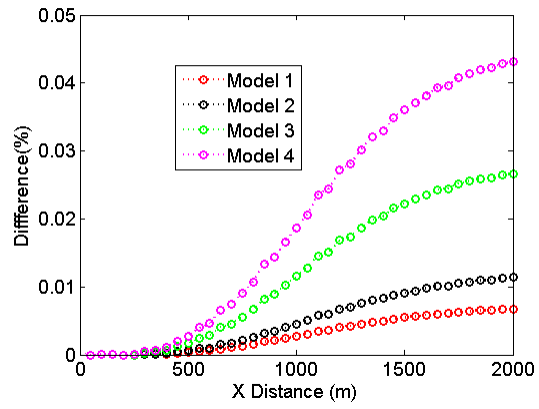
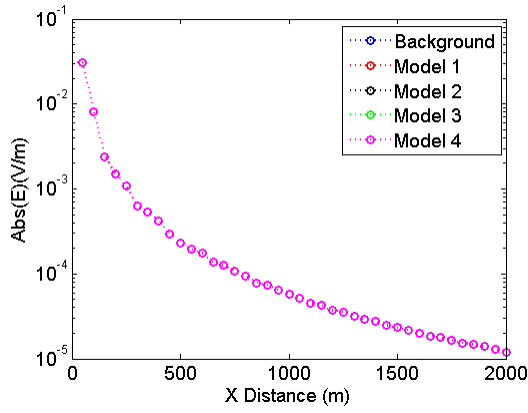
587

588

(b)

589 **Figure 7.** Electric field measurements along (a) survey line 1 and (b) survey line 2 and their relative
 590 difference with respect to the 0.005 S/m (200 Ohm-m) background response.

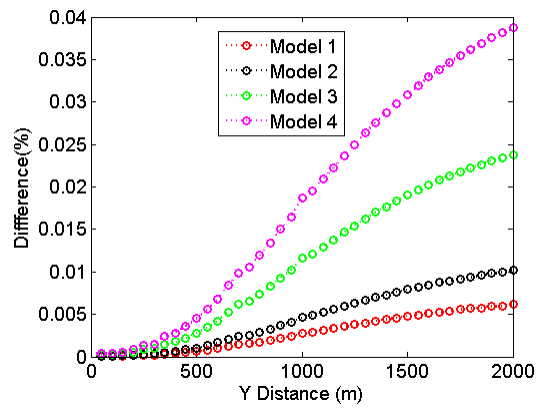
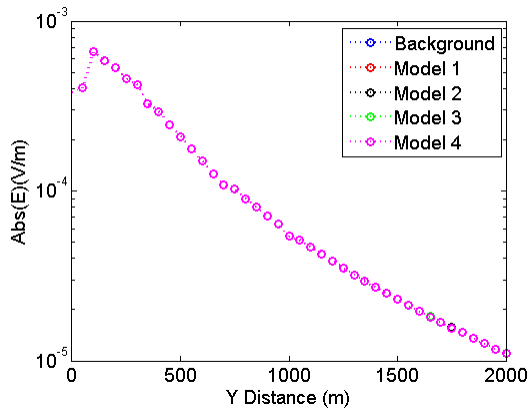
591



592

593

(a)



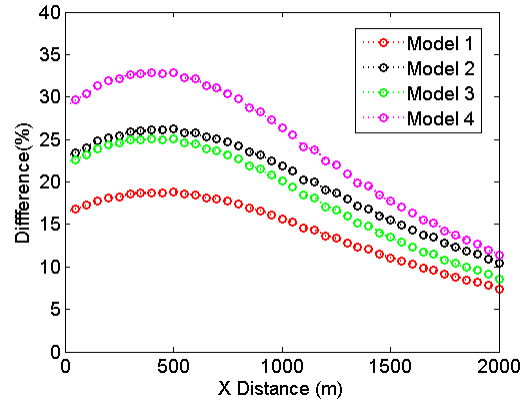
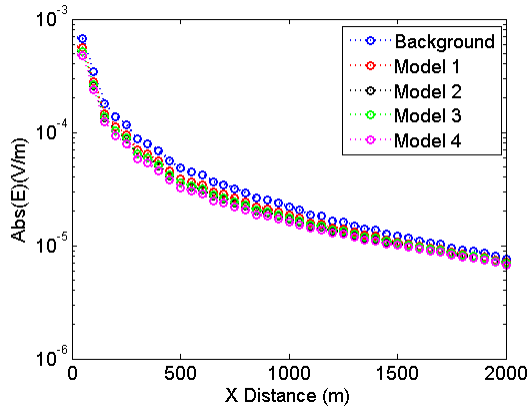
594

595

(b)

596 **Figure 8.** Electric field measurements without the steel-cased well along (a) survey line 1 and (b) survey
 597 line 2 and their relative difference with respect to the background response.

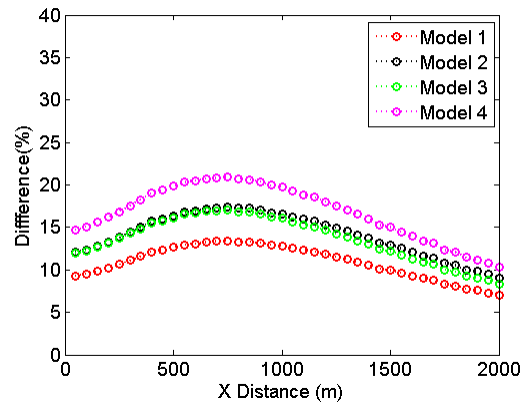
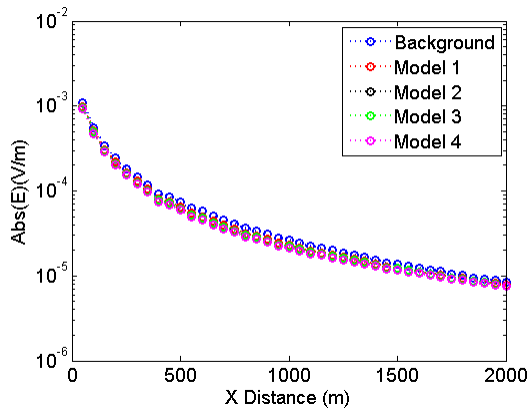
598



599

600

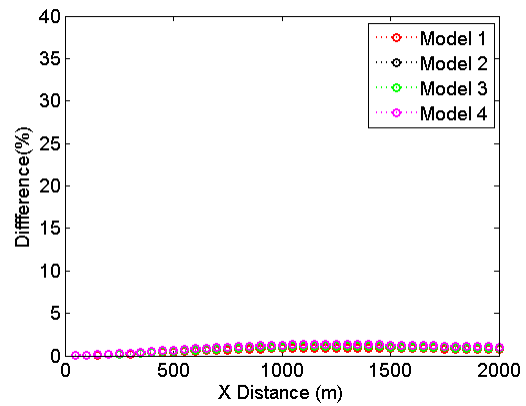
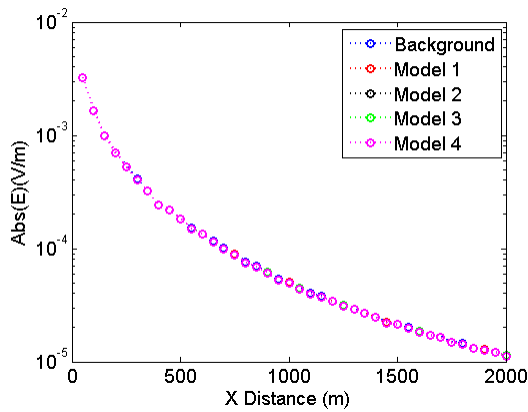
(a)



601

602

(b)



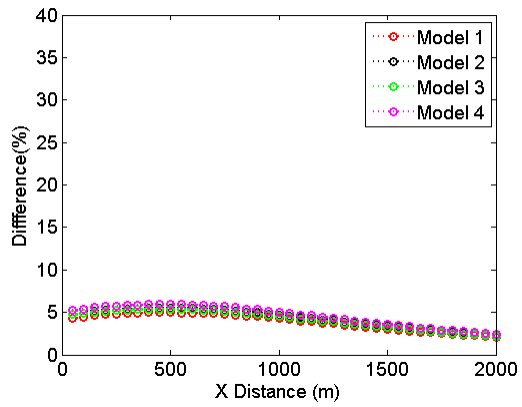
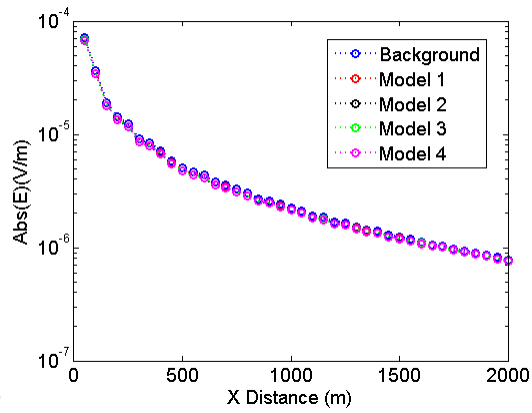
603

604

(c)

605 **Figure 9.** Electric field measurements along +x axis (survey line 1) with partially and fully damaged
 606 cased wells. (a) Intact ($5 \cdot 10^6$ S/m) casing (**Figure 5a**). (b) The corroded ($5 \cdot 10^3$ S/m) casing at $z=500$ m. (c)
 607 The completely broken casing at $z=500$ m.

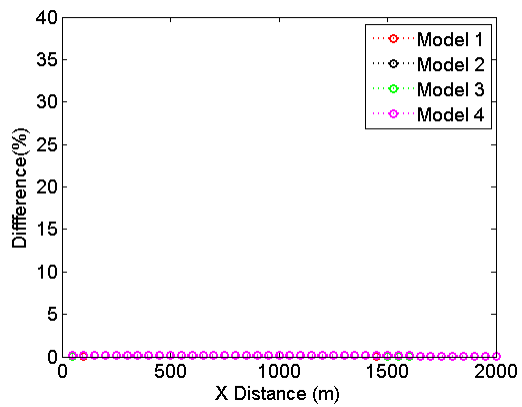
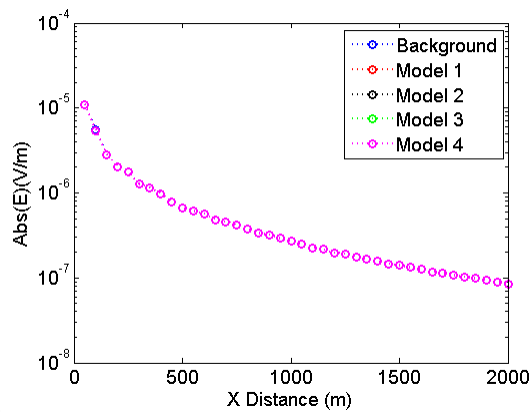
608



609

610

(a)



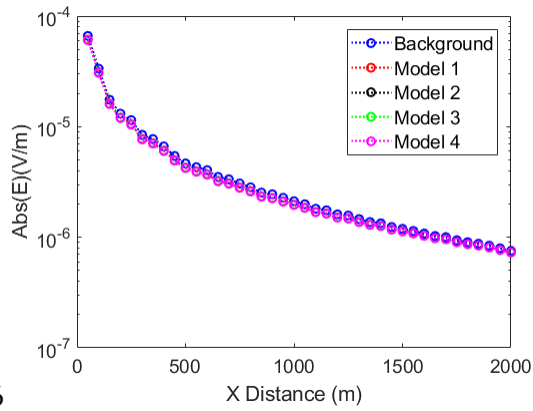
611

612

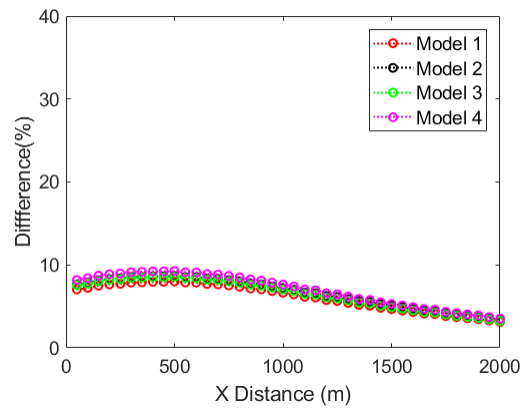
(b)

613 **Figure 10.** Electric field measurements along +x axis (survey line 1) with different background
 614 conductivity values. (a) Background conductivity= $5 \cdot 10^{-2}$ S/m. (b) Background conductivity= $5 \cdot 10^{-1}$ S/m.

615

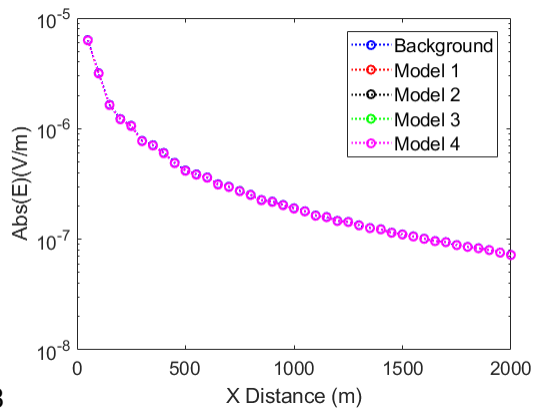


616

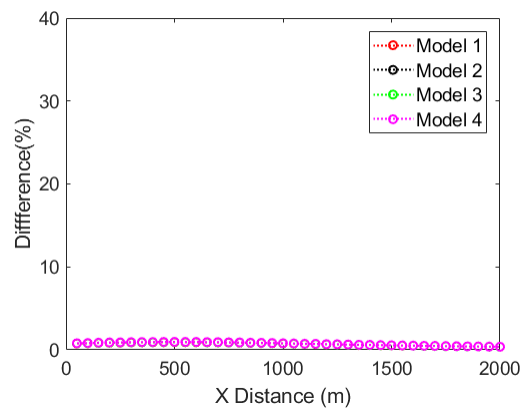


617

(a)



618

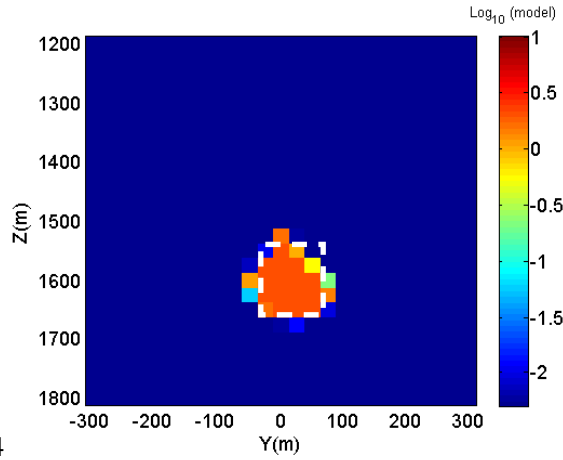


619

(b)

620 **Figure 11.** Electric field measurements along +x axis (survey line 1) with different background
 621 conductivity values. (a) Background conductivity= $5 \cdot 10^{-2}$ S/m. (b) Background conductivity= $5 \cdot 10^{-1}$ S/m.
 622 The cased well is coated with 0.2m thick 10^{-2} S/m oil-based mud.

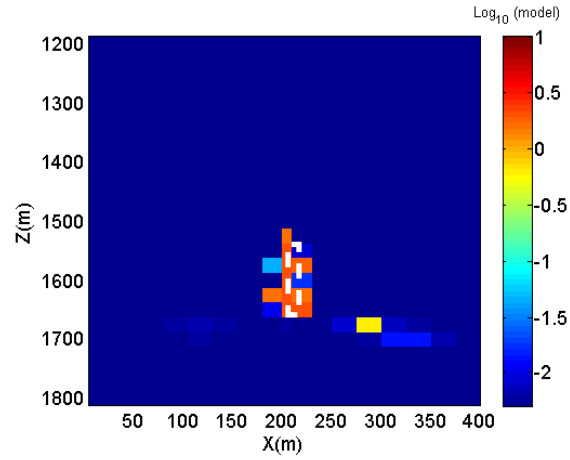
623



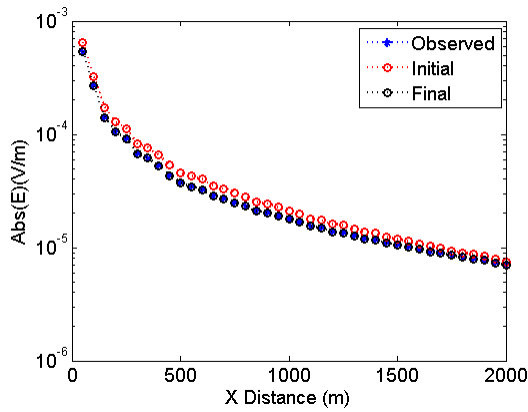
624

625

(a)



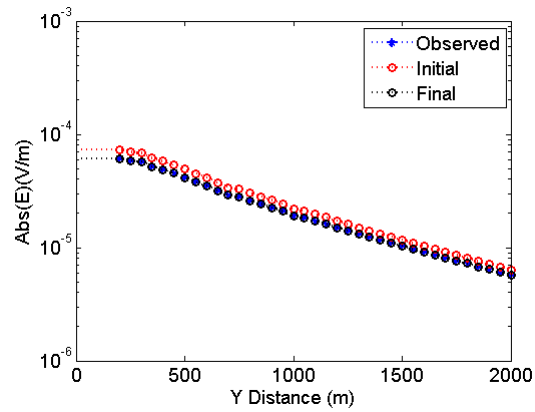
(b)



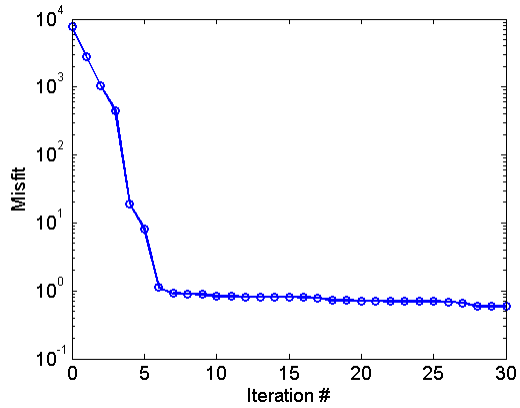
626

627

(c)



(d)

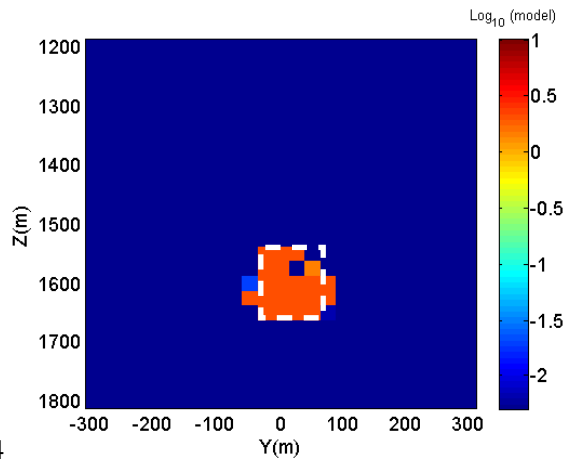


628

629

(e)

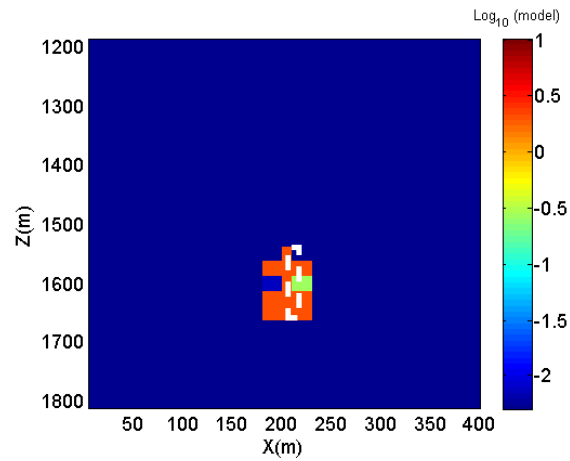
630**Figure 12.** Inversion for model 1. (a) YZ cross-sectional view at $x=200\text{m}$. (b) XZ cross-sectional view at $y=0\text{m}$. (c) Data plots along line 1 before and after the inversion. (d) Data plots along line 2 before and after the inversion. (e) Misfit as a function of inversion iteration. The white boxes in (a) and (b) indicate the true boundaries of model 1.



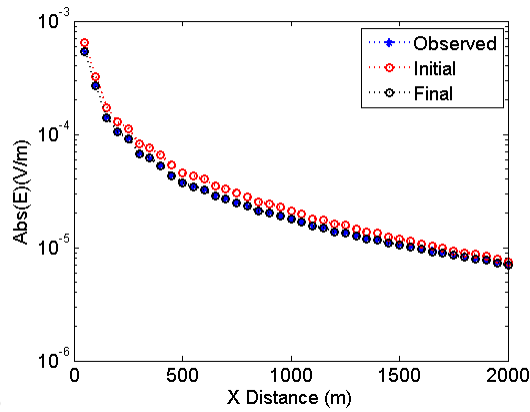
634

635

(a)



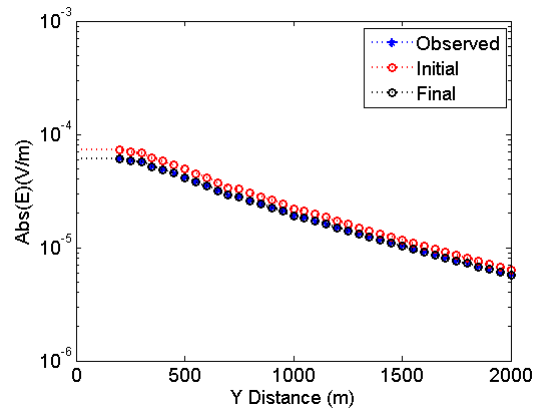
(b)



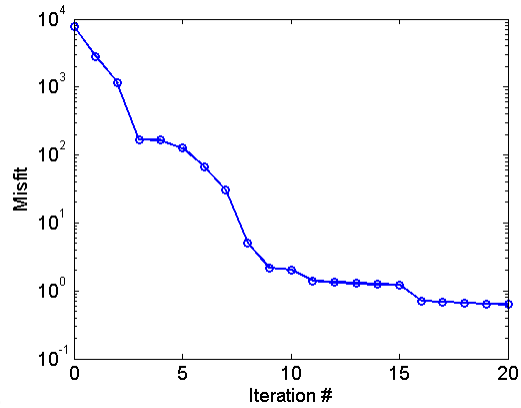
636

637

(c)



(d)

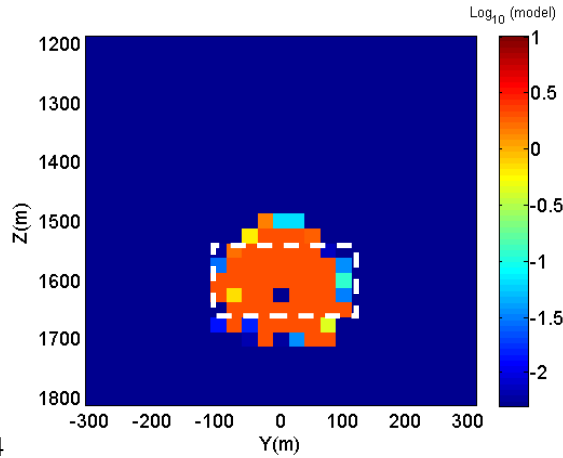


638

639

(e)

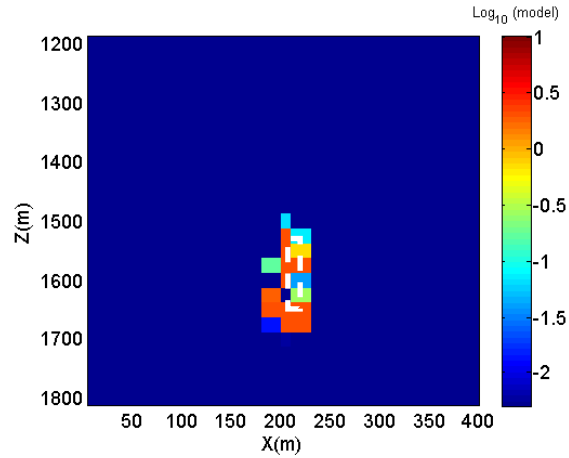
640**Figure 13.** Inversion for model 1 with the imaging domain constrained in the x-direction. (a) YZ cross-
 641sectional view at $x=200\text{m}$. (b) XZ cross-sectional view at $y=0\text{m}$. (c) Data plots along line 1 before and
 642after the inversion. (d) Data plots along line 2 before and after the inversion. (e) Misfit as a function of
 643inversion iteration. The white boxes in (a) and (b) indicate the true boundaries of model 1.



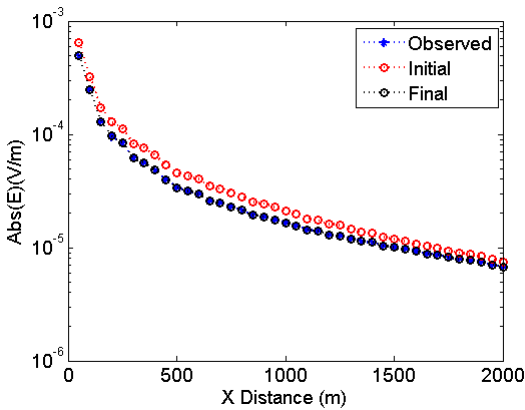
644

645

(a)



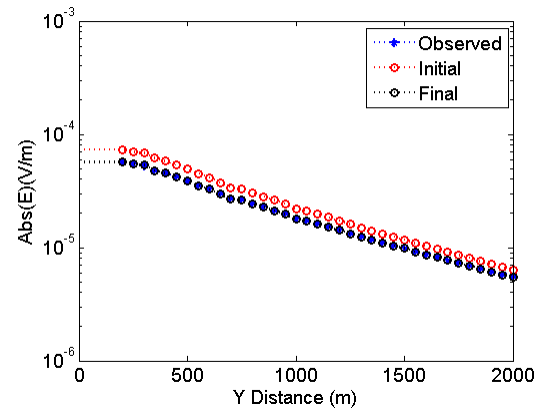
(b)



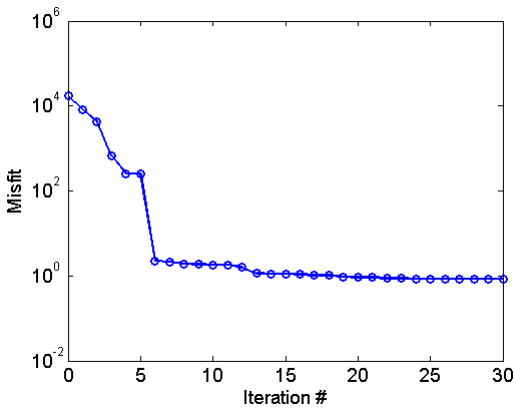
646

647

(c)



(d)

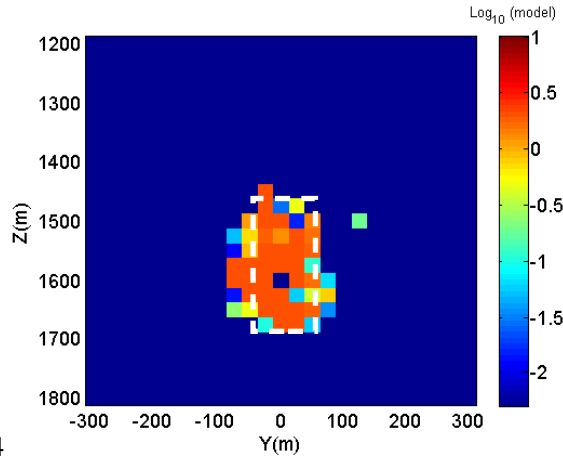


648

649

(e)

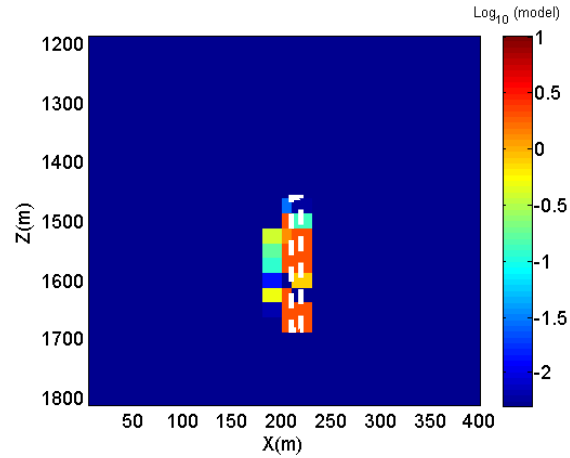
650**Figure 14.** Inversion for model 2 with the imaging domain constrained in the x-direction. (a) YZ cross-
651sectional view at $x=200\text{m}$. (b) XZ cross-sectional view at $y=0\text{m}$. (c) Data plots along line 1 before and
652after the inversion. (d) Data plots along line 2 before and after the inversion. (e) Misfit as a function of
653inversion iteration. The white boxes in (a) and (b) indicate the true boundaries of model 2.



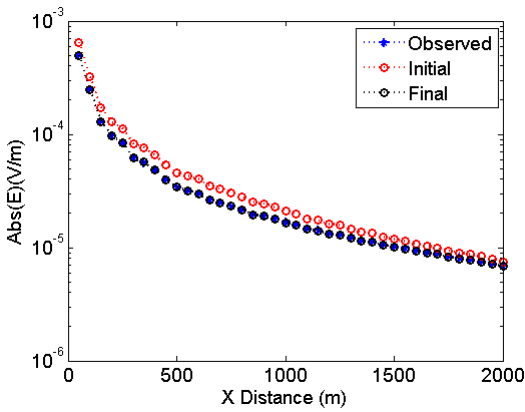
654

655

(a)



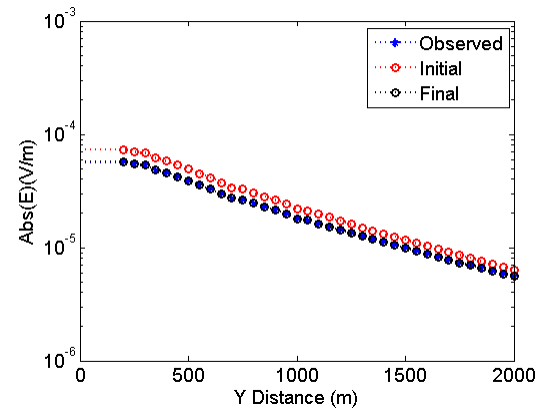
(b)



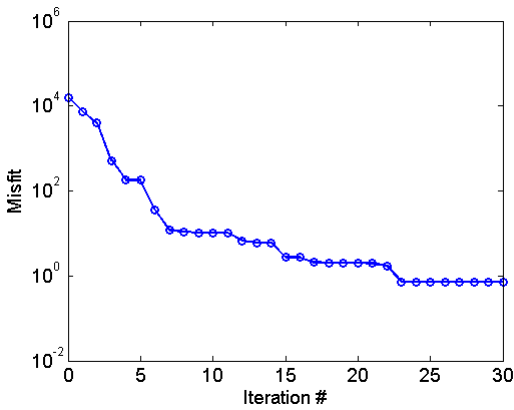
656

657

(c)



(d)

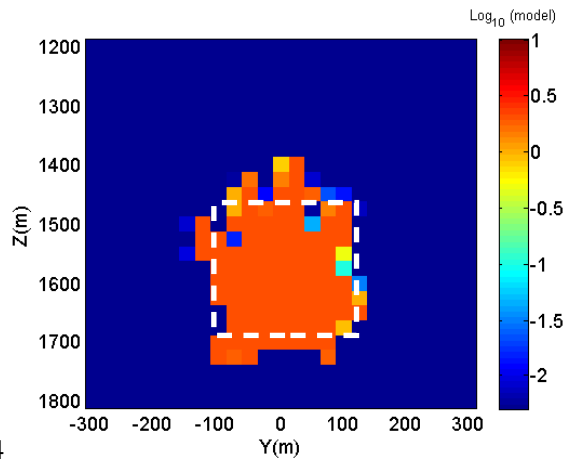


658

659

(e)

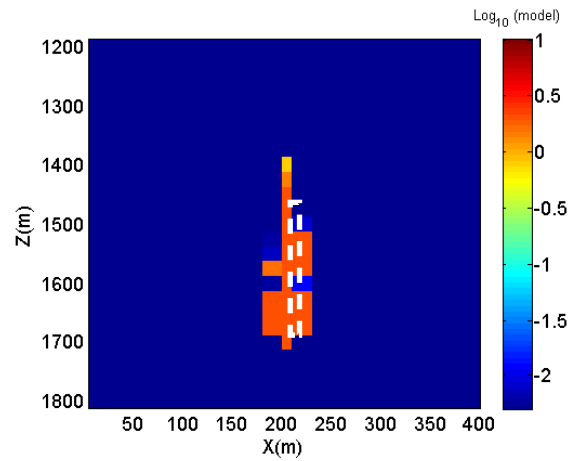
660**Figure 15.** Inversion for model 3 with the imaging domain constrained in the x-direction. (a) YZ cross-
 661sectional view at $x=200\text{m}$. (b) XZ cross-sectional view at $y=0\text{m}$. (c) Data plots along line 1 before and
 662after the inversion. (d) Data plots along line 2 before and after the inversion. (e) Misfit as a function of
 663inversion iteration. The white boxes in (a) and (b) indicate the true boundaries of model 3.



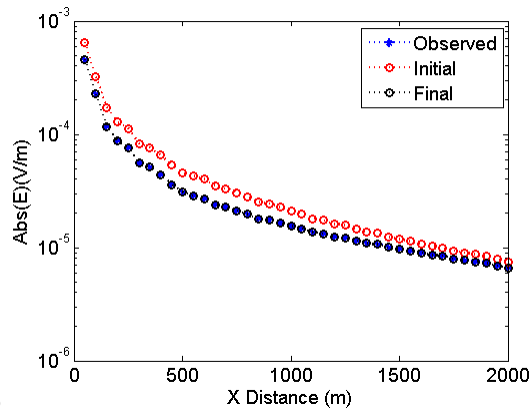
664

665

(a)



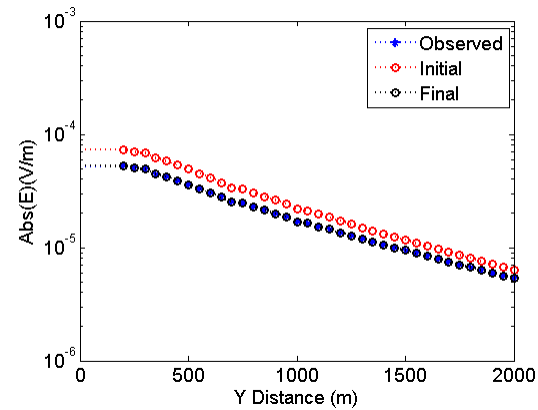
(b)



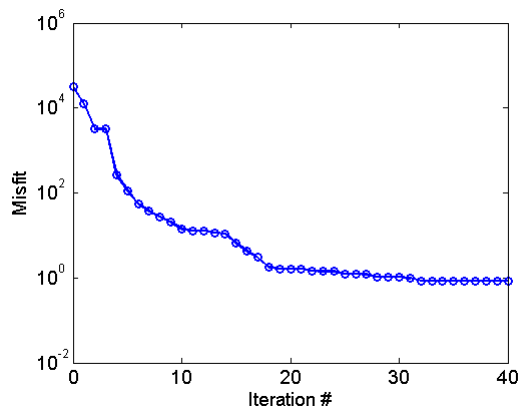
666

667

(c)



(d)

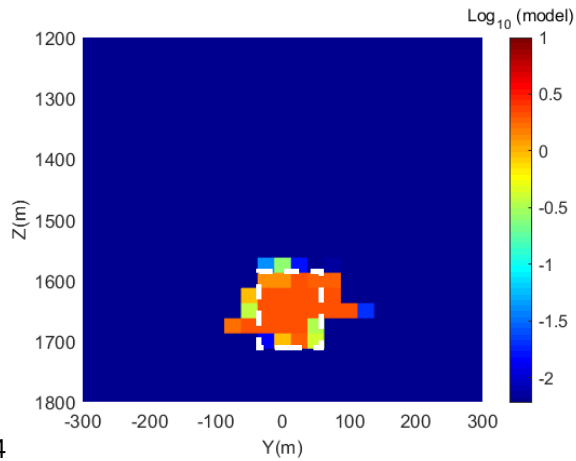


668

669

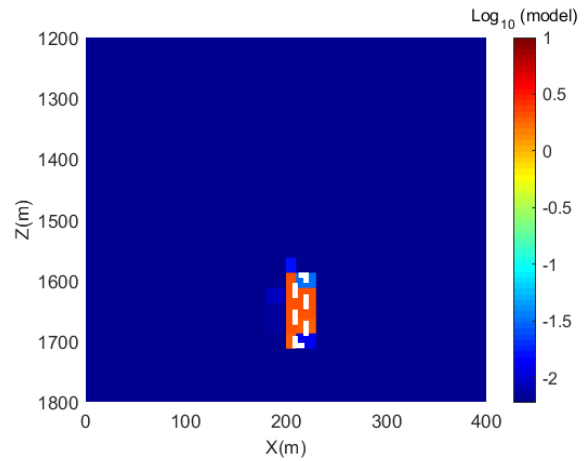
(e)

670**Figure 16.** Inversion for model 4 with the imaging domain constrained in the x-direction.. (a) YZ cross-
671sectional view at x=200m. (b) XZ cross-sectional view at y=0m. (c) Data plots along line 1 before and
672after the inversion. (d) Data plots along line 2 before and after the inversion. (e) Misfit as a function of
673inversion iteration. The white boxes in (a) and (b) indicate the true boundaries of model 4.



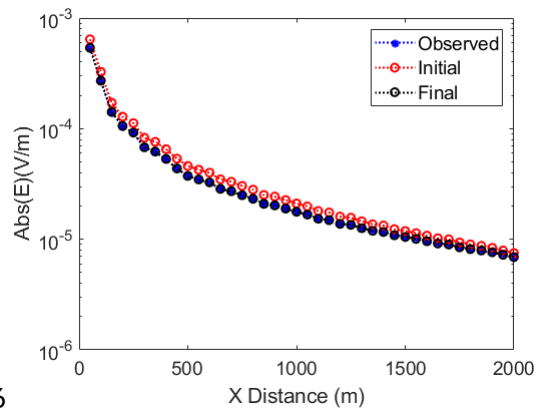
674

(a)



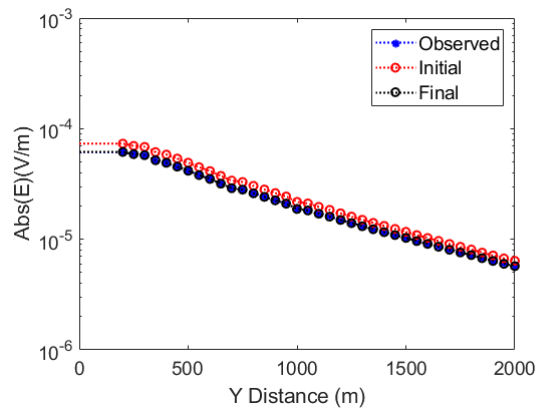
675

(b)



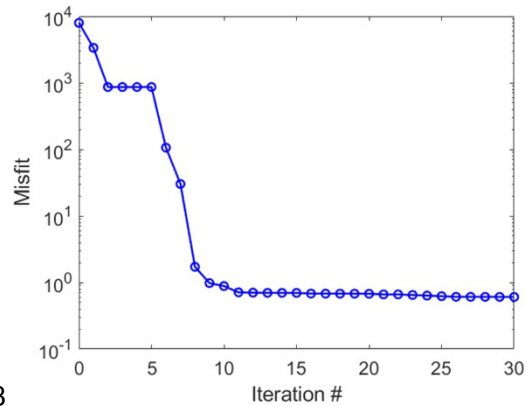
676

(c)



677

(d)



678

(e)

680**Figure 17.** Inversion for model 1 with 5% noise level. (a) YZ cross-sectional view at x=200m. (b) XZ
681cross-sectional view at y=0m. (c) Data plots along line 1 before and after the inversion. (d) Data plots
682along line 2 before and after the inversion. (e) Misfit as a function of inversion iteration.

683

87

88

684**TABLE CAPTION**

685

| HAFZ | Width (m) | Height (m) | Thickness (m) | Conductivity (S/m) |
|---------|----------------------------|-----------------------------|-----------------------|--------------------|
| Model 1 | $-62.5 \leq y \leq 62.5$ | $1537.5 \leq z \leq 1662.5$ | $200 \leq x \leq 201$ | 10 |
| Model 2 | $-112.5 \leq y \leq 112.5$ | $1537.5 \leq z \leq 1662.5$ | $200 \leq x \leq 201$ | 10 |
| Model 3 | $-62.5 \leq y \leq 62.5$ | $1462.5 \leq z \leq 1687.5$ | $200 \leq x \leq 201$ | 10 |
| Model 4 | $-112.5 \leq y \leq 112.5$ | $1462.5 \leq z \leq 1687.5$ | $200 \leq x \leq 201$ | 10 |

686

687**Table 1.** The description about the four HAFZ models.